Spin Asymmetries on the Nucleon Experiment

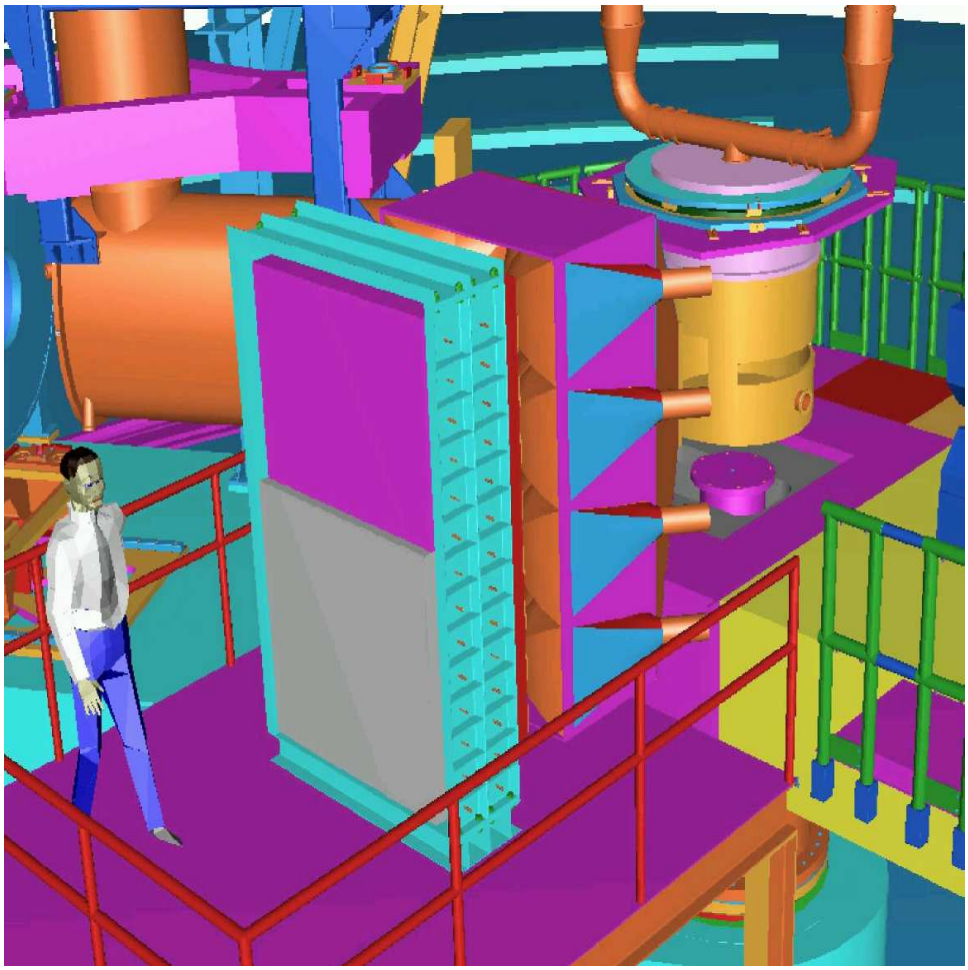

TJNAF October 7, 2003

Spin Asymmetries on the Nucleon Experiment
SANE

October 7, 2003

J.-P. Chen, R. Ent, D. Gaskell, J. Gomez, D. Higinbotham, M. Jones, D. Mack, J. Roche, G. Smith, G. Warren, B. Wojtsekhowski, S. Wood
Thomas Jefferson National Accelerator Facility, Newport News, VA

D. Day, N. Liyanage, P. McKee, O. Rondon (contact person), F. Wesselmann, H. Zhu
University of Virginia, Charlottesville, VA

T. Averett
College of William and Mary, Williamsburg, VA

E. Christy, C. Keppel
Hampton University, Hampton, VA

A. Vasiliev
Institute for High Energy Physics, Protvino, Moscow Region, Russia

T.A. Forest
Louisiana Tech University, Ruston, Louisiana

V. Kubarovsky
Rensselaer Polytechnic Institute, Troy, NY

Seonho Choi (cospokesperson), Z.-E. Meziani (cospokesperson)
Temple University, Philadelphia, PA

J. Jourdan, M. Kotulla, D. Rohe
University of Basel, Basel, Switzerland

A. Agalaryan, R. Asaturyan, H. Mkrtchyan, S. Stepanyan, V. Tadevosyan
Yerevan Physics Institute, Yerevan, Armenia

Abstract

Inclusive spin asymmetries at large x are important for understanding strong QCD in the unique, "sea-free" region, as well as for connecting experimental data to the moments of polarized Parton Distribution Functions calculated in Lattice QCD. We propose a new experimental technique with revolutionary increase in Figure of Merit which is required to measure precise, inclusive spin asymmetries on the proton at large x. Using the highest available JLab beam energy, the UVa polarized NH_3 target will be employed at $8.5 \cdot 10^{34}$ proton-luminosity with a 194 msr electromagnetic calorimeter instrumented for at least 1000:1 pion rejection. In the DIS region, A_1^p and g_2^p will be determined up to $x = 0.63$ assuming 6 GeV beam energy. The quality of the data will enable us to study the Q^2 dependence of g_1 and g_2 as well as their third moments. From these quantities, we will be able to determine d_2, one of the cleanest signatures of higher twist effects, with less than one-half of the existing uncertainty. Data taken simultaneously in the resonance region at somewhat lower x and Q^2 will be used to see if suitably averaged spin structure functions yield the DIS result, in what W ranges, and with what accuracy. If the "spin duality" hypothesis turns out to be a useful approximation with boundable errors, it could potentially be used to extract A_1^p and A_2^p to x as large as 0.80. With the emphasis on measurements with the target polarization transverse to the beam, our results will complement the existing EG1b run group data of CLAS, which is longitudinal target polarization.

Executive Summary

The large x region is fascinating because it provides a window on proton structure in a regime where the sea quarks have been stripped away. One may hope that simple models can be applied to these "naked protons", potentially leading to insights into strong QCD complementary to those obtained a generation ago from Constituent Quark Model descriptions of the baryon mass spectrum. Nucleon spin asymmetries at large x may not only yield clues about $SU(6)$ (spin-flavor) symmetry breaking in confinement QCD, but are essential for the determination of all but the first moment of the spin structure functions. These moments are the natural connection between experiment and Lattice QCD, since Lattice calculations do not directly determine spin observables like A_1^p but only the lowest several moments of the various polarized and unpolarized parton distribution functions (PDF's).

Lattice QCD collaborations hope to begin calculating the moments of these PDF's with near-physical pion masses in the next few years employing Teraflop·Year computing resources. Results are available today using 0.1 Teraflop·Year computations which unfortunately require significant extrapolations to the chiral limit.[1] However, the paucity of accurate data at high x means that there will generally be significant ambiguities in relating spin structure function observables to Lattice QCD moments. One certain way to remove this ambiguity is with precise data at large x. Unfortunately, the probability of finding a single quark with a large fraction of the nucleon's longitudinal momentum is small, so large x measurements are often not merely statistics-limited but statistics-starved. An important exception are the three forthcoming A_1^n points from Hall A, which clearly show for the first time that A_1^n at large x is non-zero and rising.

Although the world dataset for A_1^p is in better shape than that of A_1^n, the trend of the data in the limit $x \to 1$ is not clear, and is completely inadequate for estimating all but the first moment of A_1^p. Our goal is to obtain precision A_1^p and A_2^p results at the largest possible x. However, a thorough program of A_1^p and A_2^p measurements at large x, including tests of the W dependence, would consume thousands of hours of beam time using traditional techniques. For that reason, we are proposing a new experiment with a revolutionary increase in Figure of Merit for making high x spin structure function measurements. The experiment is called SANE (**S**pin **A**symmetries on the **N**ucleon **E**xperiment), and is based on a 194 msr electron detector viewing the UVa polarized nucleon target operating at $8.5 \cdot 10^{34}$ proton-luminosity. For our first measurement, we request 654 hours to make precise DIS measurements of A_1 and A_2 on the proton for x to 0.63. In this amount of time, it will also be possible to test whether, or to what accuracy, suitably averaged measurements in the resonance region reproduce the DIS result for A_1^p (i.e., so-called "spin duality"). If the errors in applying spin-duality can be reliably bounded, this would make it possible to determine A_1^p to x as large as 0.80.

The g_2 SSF has twist-2 (from g_1) and twist-3 components, which can be separated with a precision measurement of this SSF at $x > 0.3$. The third moment of the twist-3 part is proportional to the corresponding twist-3 d_2 matrix element that represents quark-gluon interactions and has been calculated in Lattice QCD, QCD sum rules and other theoretical models. The proposed SANE g_2 measurement will extract d_2 with unprecedented precision at several values of $Q^2 < 6$ GeV/c^2 for a conclusive determination of this fundamental quantity. Only SANE is capable of such result at the proposed kinematics.

1 Introduction and Motivation

The nucleon spin structure functions (SSF) describe, as their name implies, fundamental properties of the nucleon because they are directly related to the quark helicity distribution and quark-gluon interactions. The SSF's form the antisymmetric part of the hadronic tensor in lepton-nucleon scattering [2, 3]. As a consequence, the SSF's can be measured in inclusive inelastic scattering of polarized leptons on polarized nucleons.

When the incident lepton helicity is aligned with the target nucleon spin, the cross section is dominated by g_1, the longitudinal SSF. g_1 can be interpreted in the parton model in terms of helicity densities of the different quark flavors, weighted by the square of the quark charges e_i:

$$g_1(x,Q^2) = \frac{1}{2}\sum\nolimits_i e_i^2[q_i^{\uparrow}(x,Q^2) - q_i^{\downarrow}(x,Q^2)], \qquad i = u, \bar{u}, d, \bar{d}, s, \bar{s}, ... \tag{1}$$

where $x = Q^2/(2M\nu)$ is the Bjorken scaling variable, $Q^2 = -q_\mu^2$ is the four-momentum transfer squared, M is the nucleon mass and $\nu = E - E'$ is the energy loss of a lepton with initial energy E.

When the target spin is perpendicular to the lepton helicity, the cross section is dominated by g_2, the transverse SSF. g_2 probes a combination of transverse and longitudinal parton polarization distributions inside the nucleon. This SSF is understood to be made up of two components: a twist-2 part g_2^{WW} and a mixed twist-2/twist-3 part $\overline{g}_2$ [4, 5, 6]

$$g_2(x,Q^2) = g_2^{WW}(x,Q^2) + \overline{g}_2(x,Q^2). \tag{2}$$

The SSF's have been extensively measured in a broad kinematic range, from the deep inelastic scattering regime (DIS) [7, 8, 9, 10, 11, 12, 13, 14, 15, 16] through the nucleon resonances down to the pion production threshold [17, 18, 19, 20, 21, 22], with both real [23, 24] and very high Q^2 virtual photons. From those measurements we have learned that the quarks contribute at most only 30% of the nucleon spin, and that there are small but non-negligible quark - gluon interactions in the region of $0.2 \leq x \leq 0.4$.

The focus of the DIS SSF program in the past has been the determination of the moments of the SSF's which are related to quark matrix elements that can be calculated from basic QCD principles. Thus, the difference of the first moments of the proton and neutron longitudinal SSF's g_1^p and g_1^n is the fundamental Bjorken sum rule,

$$\Gamma_1^p(Q^2) - \Gamma_1^n(Q^2) = \int_0^1 (g_1^p(x,Q^2) - g_1^n(x,Q^2))dx = \frac{1}{6}\frac{g_A}{g_V}C_{NS}(\alpha_s) \tag{3}$$

which has now been verified experimentally to better than 10%. Similarly, the third moment of the mixed twist $\overline{g}_2(x,Q^2)$ is related by the operator product expansion (OPE) to the twist-3 quark matrix element d_2, if the small twist-2 quark mass dependent term is neglected,

$$\int_0^1 x^2\overline{g}_2(x,Q^2)dx = \frac{1}{3}d_2(Q^2). \tag{4}$$

For the low moments of the SSF's, such as those involved in the Bjorken or Ellis-Jaffe sum rules, the important contributions come from the small x region, which has been explored in DIS with very high beam energies at CERN, SLAC and HERMES. On the other hand, the

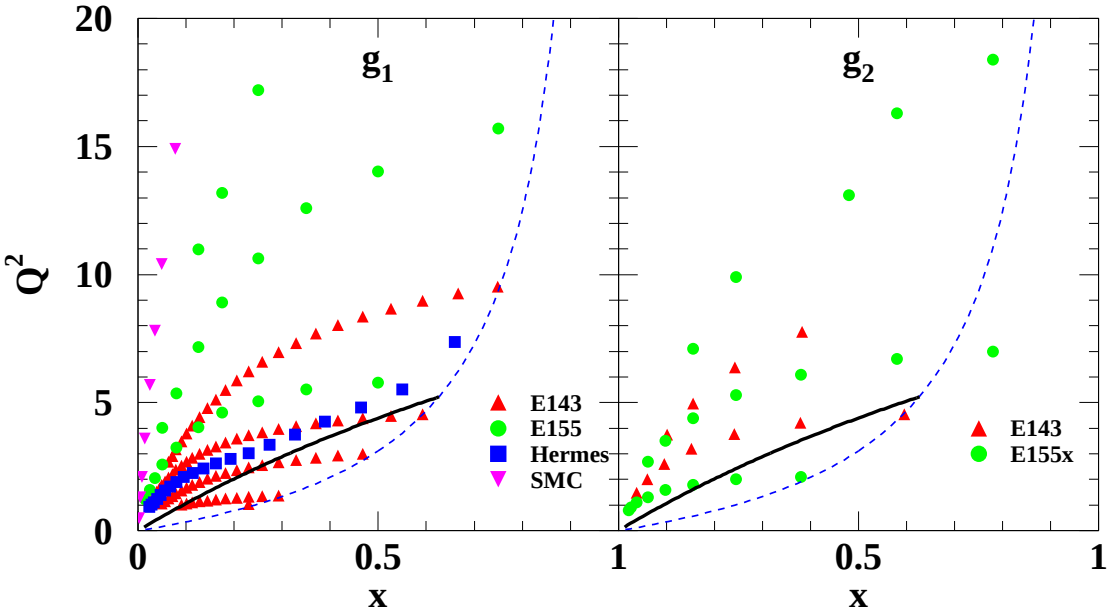

Figure 1: Kinematics of DIS g_1^p(left) and g_2^p(right) measurements for 1 GeV^2 $\leq Q^2 \leq$ 20 GeV^2. The region of $W > 2$ GeV lies to the left of the dashed (blue) curve. The thick black line represents the maximum $Q^2(x)$ achievable with 6 GeV and scattering angles of less than 45°.

high x region has not been explored in detail because the nucleon resonances are dominant at the momentum transfers that can be accessed with adequate statistical precision in existing facilities: *the DIS process in the high x region is confined to very high values of Q^2*. The situation is clearly illustrated in Figure 1, which shows the kinematics of the world data for the proton g_1 and g_2 SSF's.[1] As a result, the way in which the SSF's approach $x = 1$ is only now beginning to be investigated; for example in the recent Hall A A_1^n experiment [21]. This kinematic region is of great interest for several reasons:

- The calculations of the SSF moments are based on extrapolations of fits to the data from the regions where they have been measured to both the $x = 0$ and the $x = 1$ ends of the Bjorken variable range [11, 14]. For $Q^2 \leq$ 5 GeV^2, which corresponds to the value commonly used to evaluate the moments, the measured DIS region ends below $x \sim 0.6$. In the past, arguments based on quark counting rules [25] have been used to estimate the contributions of the unmeasured $0.6 < x \leq 1$ region. This procedure involves a double extrapolation that is seldom explicitly stated, to $x = 1$ along the constant Q^2 value at which the moments are evaluated, extending into a region where there is no data and where the kinematics corresponds to invariant mass $W < 2$ GeV. However, for the higher moments, *it is precisely*

[1] It is worth noting that there is significantly less data for g_2 than for g_1.

this region that has the greatest weight. As a result, there is a significant model dependence in the quoted numbers for quantities such as d_2, and to some extent for the Bjorken sum rule evaluated at $Q^2 \leq 5$ GeV^2.

• The spin asymmetry A_1 is related to the SSF's by way of the unpolarized SF $F_1(x,Q^2) = \frac{1}{2}\sum_i e_i^2[q_i^{\uparrow}(x,Q^2) + q_i^{\downarrow}(x,Q^2)]$. In terms of the scaling form of the SF's

$$A_1(x,Q^2) = \frac{1}{F_1(x,Q^2)}\Big(g_1(x,Q^2) - \gamma^2 g_2(x,Q^2)\Big), \tag{5}$$

where $\gamma^2 \equiv Q^2/\nu^2$. The contributions of the quark sea and gluons to A_1 decrease rapidly with increasing x. As a result, $A_1(x >\sim 0.3)$ is dominated by the valence quarks. Quark models of the nucleon (which involve only valence quarks) such as $SU(6)$ have definite predictions [26] about the value of $A_1(x=1)$: the naïve $SU(6)$ model predicts A_1^p=5/9, but $SU(6)$ broken by hyperfine quark interactions predicts $A_1^p(x=1) = 1$. The different flavor dependence of A_1 for protons and neutrons can be exploited to separate the u and d quark components, and the results can be extended in turn to test the quark model predictions about the ratio of the neutron to proton cross sections, $F_2^n(x)/F_2^p(x)$ at $x = 1$.

• Perturbative QCD predicts [27] that $A_1^p(x=1) = 1$, based on helicity conservation of the leading quark. The approach to $x = 1$ predicted by pQCD is based on the connection between g_1 and F_1, which is not the same as that of broken $SU(6)$, which depends on the spin flip probability of relativistic quark models [26]. The current world data sample on A_1^p for $W \geq 2$ GeV shown in Fig. 2 does not have adequate precision to constrain $A_1^p(1)$.

• A more careful look at the connection between A_1 and g_1 given in Eqn.(5) reveals that the supposed independence of A_1 on Q^2 may really apply only at very small x or at very large Q^2. The kinematic factor $\gamma^2 = 4x^2M^2/Q^2$ is negligible ($\gamma^2 \leq 0.1$) for $x \geq 0.3$ only for values of Q^2 that start at 3 (GeV/c)^2 and increase up to 35 (GeV/c)^2 at $x = 1$. Neglecting the small twist-3 $\overline{g}_2(x,Q^2)$ term, the twist-2 part of g_2, $g_2^{WW}(x) = -g_1(x) + \int_x^1 (g_1(y)/y)dy$ contributes to A_1 as

$$A_1(x,Q^2) = \frac{1}{F_1}\Big(g_1(x,Q^2)(1+\gamma^2) - \gamma^2\int_x^1 \frac{g_1(y,Q^2)}{y}dy\Big),$$
$$A_1(1,Q^2) = \frac{g_1(1,Q^2)}{F_1(1,Q^2)}(1 + \frac{4M^2}{Q^2}). \tag{6}$$

This result implies that A_1 is not independent of Q^2 [28], unless g_1/F_1 has the exact inverse Q^2 dependence of the kinematic factor, or else, that the neglected $\overline{g}_2(x,Q^2)$ component (significantly not zero only at intermediate x,) mysteriously conspires to cancel all remaining dependencies to keep A_1 constant. Incidentally, Eqn.(6) can be used to get $A_1(x=1)$ from extrapolations of global fits to g_1/F_1 [11, 14, 29].

• The SSF's receive increasing contributions from higher-twist terms as x approaches 1 at constant Q^2. The higher-twists represent increasing interactions among the partons, which can be related to quark matrix elements that can also be calculated in Lattice QCD. For example the twist-3 d_2 matrix element represents quark-gluon interactions that can be computed in Lattice QCD. SLAC E155x has measured $g_2(x,Q^2)$ for protons and deuterons, and calculated $d_2(Q^2$=5 GeV$^2)$ with the assumption that the extracted $\overline{g}_2$ is independent of Q^2. However, the third moments of g_2 from E155x have contributions from only four

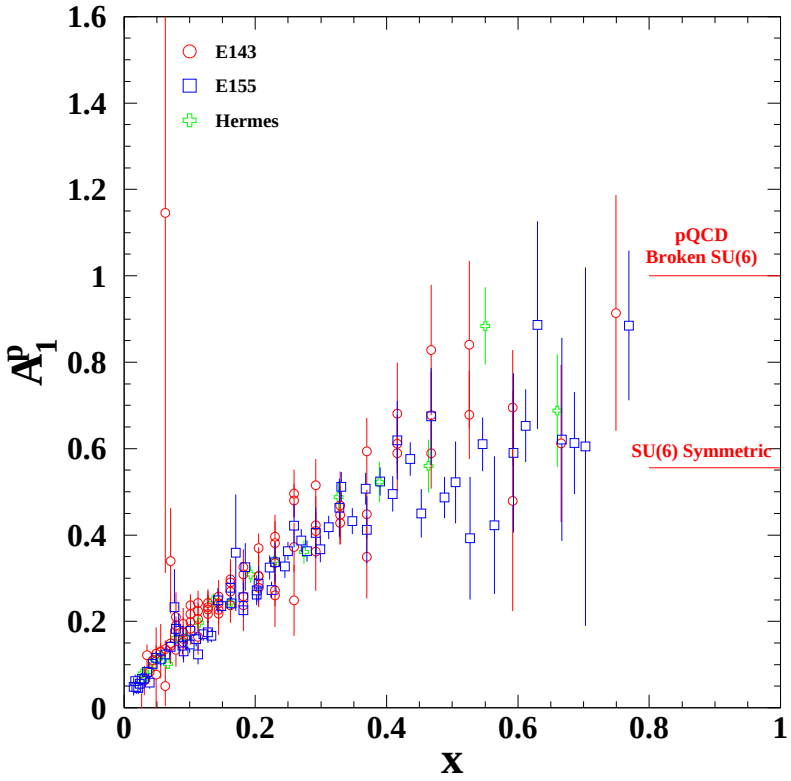

Figure 2: DIS $A_1^p(x, Q^2)$ data. The pQCD and naïve $SU(6)$ model values for A_1^p(x=1) are indicated. The data are shown at the measured Q^2, not evolved to a constant value.

measured points above $x = 0.3$, which make up 90% of the integral. Improvements in the determination of d_2 can only come from more precise data at high x, in particular in the region between $0.3 \leq x \leq 0.8$, where the largest difference between the twist-2 part of g_2 and the measured g_2 is observed (the small – and decreasing – magnitude of $\overline{g}_2$ makes the $x > 0.8$ region less important).

• The SLAC experiments have obtained g_2 data over a broad range of Q^2. However, there remain substantial gaps in the region $0.3 < x$ where the data tend to concentrate above $Q^2 \sim 5$ GeV^2. Precision g_2 data for Q^2 up to ~ 6 GeV^2 would significantly improve our knowledge of the Q^2 dependence of g_2 to test against models of higher-twists [30], which are expected to be more important in this region.

Similarly the twist-4 f_2 matrix element represents quark-quark interactions, and reflects the higher twist corrections to the individual proton and neutron moments and in consequence, to the Bjorken sum rule [31]

$$\int_0^1 g_1(x, Q^2)dx = a_0 + \frac{M}{9Q^2}(a_2 + 4d_2 + 4f_2) + O\Big(\frac{M^4}{Q^4}\Big). \tag{7}$$

These matrix elements are related to the higher moments of the SSF's, which have a strong dependence on the high x contributions.

The above considerations make it clear that precise measurements of the SSFs in the region of $x > 0.5$ are required for further progress in our understanding of the nucleon and the interactions of its components. JLab is the only facility in the world where these measurements can be carried out, because of the concurrence of three critical factors:

– the high polarization CEBAF beam;

– the very large solid of the proposed angle Hall C Čerenkov plus calorimeter detector system, BETA ("**B**ig **E**lectron **T**elescope **A**rray"), which makes possible high statistics measurements at $Q^2\sim$ 5 GeV^2 in reasonable amounts of run time;

– the open geometry of the UVa solid polarized target, that allows for flexible relative orientations of the beam helicity and the target spins, coupled with the high proton polarizations($\geq$ 75% average) that it can attain.

We propose to carry out one such measurement using the Jefferson Lab CEBAF and Hall C facilities and the UVa polarized target. The goal of the proposal is to extract the proton A_1 limited by systematic errors and a simultaneous statistics limited measurement of g_2^p in the range $0.3 \leq x \leq 0.8$ at an average Q^2=4.5 (GeV/c)^2 in a model-independent fashion, from the measurement of two asymmetries for two different orientations of the target magnetic field relative to the beam direction. The scattered electrons will be detected in the BETA detector. The measured A_1 and g_2 will be used directly to:

- study their Q^2 dependence at fixed x in both the DIS and resonance region,
- probe the approach of A_1 to $x = 1$ at constant Q^2 in order to test quark models and pQCD, combining SANE's results with the world data sample,
- determine $\overline{g}_2$ with high precision in the critical region $0.3\leq x \leq 0.8$ at fixed Q^2, and compute d_2 combining SANE and SLAC data.
- extract better values of g_1 from A_1 and A_2 with the aid of the unpolarized structure functions F_2 and R to further improve the calculation of moments,
- conduct a limited test of local duality for the polarized SSF's down to the second resonance region.

In what follows we discuss the choice of kinematics and technique, the detectors, and their response to electrons and background, the polarized target and auxiliary equipment, and we give estimates of the expected count rates, statistical precision and systematic errors. We conclude with a summary run plan and beam request.

2 Method

As stated in the Introduction, the SSF's contribute to the polarized lepton-polarized nucleon cross section. In order to separate the unpolarized SF's from the SSF's, the difference of cross sections at a fixed value of the angle between the beam helicity and the target spin is formed. The resulting expression for the cross section difference is given by [2, 3, 32]

$$\Delta\sigma = \frac{4\alpha E'}{Q^2 E}\Big[M(E\cos\theta_N + E'\cos\alpha)G_1 + 2EE'(\cos\alpha - \cos\theta_N)G_2\Big] \tag{8}$$

$$\cos\alpha = \sin\theta\sin\theta_N\cos\phi_N + \cos\theta\cos\theta_N$$

where θ is the lepton scattering angle and θ_N, ϕ_N are the spherical angles between the beam helicity and the target nucleon spin (beam along the z axis). In the scaling limit

$$\lim_{Q^2,\nu\to\infty}(M\nu)MG_1(Q^2,\nu)=g_1(x), \qquad \lim_{Q^2,\nu\to\infty}(M\nu)\nu G_2(Q^2,\nu)=g_2(x). \tag{9}$$

The conventional approach to extract g_1 and g_2 is to measure an asymmetry instead of the cross section difference. This procedure reduces the dependence on hard-to-measure quantities such as the detector acceptances and efficiencies. Two asymmetries are usually measured, with $\theta_N = 0$ (beam parallel to the polarized target field) and $\theta_N = \pi/2$ (beam perpendicular to the target field). The physics quantities of interest are related to the measured asymmetries (known as $A_{||}$ and $A_\perp$, $A = (\sigma^{\uparrow\uparrow} - \sigma^{\uparrow\downarrow})/(\sigma^{\uparrow\uparrow} + \sigma^{\uparrow\downarrow})$) by expressions that involve kinematical factors, as well as the unpolarized SF $R(x,Q^2) = \sigma_L/\sigma_T$:

$$\begin{aligned} A_1 &= \frac{C}{D}\Big(A_{||} - dA_\perp\Big) \\ A_2 &= \frac{C}{D}\Big(c'A_{||} + d'A_\perp\Big) \end{aligned} \tag{10}$$

where $C = 1/(1+\eta c')$; $\eta = \epsilon\sqrt{Q^2}/(E-\epsilon E')$; $c' = \eta(1+\epsilon)/(2\epsilon)$; $\epsilon^{-1} = 1 + 2[1 + (\nu^2/Q^2)]\tan^2(\theta/2)$ is the usual longitudinal polarization of the virtual photon; $D = (1 - \epsilon E'/E)/(1+\epsilon R)$ is the virtual photon depolarization factor which depends on R; $d' = 1/\sqrt{2\epsilon/(1+\epsilon)}$; and $d = \eta d'$.

The spin asymmetries A_1, A_2 are related to virtual photon absorption cross sections $\sigma^T_{1/2}, \sigma^T_{3/2}$, $\sigma^{TL}_{1/2}$ for photon helicities $+1$, -1, 0

$$A_1 = \frac{\sigma^T_{1/2} - \sigma^T_{3/2}}{2\sigma^T}, \qquad A_2 = \frac{\sigma^{TL}}{2\sigma^T}, \tag{11}$$

where $2\sigma^T = \sigma^T_{3/2} + \sigma^T_{1/2}$. The connection between A_1 and the scaling form of the SSF's has been shown in equation (5). The corresponding equation for A_2 is

$$A_2(x,Q^2) = \frac{\gamma}{F_1(x,Q^2)}\Big(g_1(x,Q^2) + g_2(x,Q^2)\Big). \tag{12}$$

The price paid in the asymmetry method is the introduction of the unpolarized SF's F_1 and R. F_1 has not been measured directly, only F_2, which is related to F_1 by

$$F_1(x,Q^2) = F_2(x,Q^2)\frac{1+\gamma^2}{2x(1+R(x,Q^2))} \tag{13}$$

An additional 2-3% systematic error in g_1 is introduced by the need to use F_2 and R.

The SSF's g_1 and g_2 can be obtained directly from the measured asymmetries $A_{||}$ and $A_\perp$ or, solving Eqn.. (5) and (12), from A_1 and A_2

$$\begin{aligned} g_1 &= \frac{F_2}{2x(1+R)}(A_1 + \gamma A_2) \\ g_2 &= \frac{F_2}{2x(1+R)}(-A_1 + \frac{A_2}{\gamma}) \end{aligned} \tag{14}$$

In practical terms, the optimum angles θ and θ_N for extracting the SSF's or the spin asymmetries are dictated by the kinematic region to be studied and the capabilities of the available equipment. To extract A_1 and g_2 in the DIS region at the highest x possible, we plan to use the full 6 GeV beam energy, combined with the largest scattering angle at which a measurement of the asymmetries with comparable statistical and systematic errors can be done in about 300 h at 100% efficiency. Our count rate estimates show that angle to be about 40°.

We will measure both $A_{\|}$ and $A_{\perp}$ to extract A_1 and g_2. There is a relative dearth of perpendicular field measurements, as seen in Fig. 1, so SANE will focus on these to expand our general body of knowledge of SSF's. As the perpendicular asymmetries are smaller than the parallel ones, we will spend roughly twice the time in the perpendicular field direction than in the parallel. This allotment of time allows us to extract g_1 and g_2 with statistical uncertainties comparable to the systematics.

The configuration of the target magnet coils precludes the use of $\theta_N = \pi/2$, so a near perpendicular asymmetry at $\theta_N = 80°$ will be measured. This angle is only somewhat (about 8%) less favorable than $\pi/2$.

Testing the actual Q^2 dependence of A_1 and g_2 becomes possible with the significant statistical precision expected from our measurements. To make this test as meaningful as possible and to study the x dependence at constant Q^2 over the broadest (x, Q^2) range without resorting to QCD evolution or interpolations/extrapolations, we plan to make a second measurement at 4.8 GeV beam energy and 40°. Figure 3 illustrates the region of the (Q^2,x) plane that can be studied with the two beam energies. With the increased counting rates at this lower average Q^2 measurement, similar statistical precision as that at 6 GeV can be obtained in about two-thirds the time. The total time for the two energies plus operational overhead is 654 h (27 d) at 100% efficiency.

The measurements at both energies extend into the region of the resonances down to $W \sim 1.4$ GeV. The resolution in W and the achievable statistical precision in this region will allow for a limited test of polarized local duality, possibly extending at the same time the measured x range of A_1 and A_2 close to $x = 0.8$.

3 Experimental Setup

The experimental setup consists of the UVa polarized proton target, a total absorption electron telescope, the High Momentum Spectrometer (HMS), and the Hall C beam line with its now-standard augmentations to allow for 50-100 nA operation and several degrees of beam deflection by the target's magnetic field. The SANE setup is shown in Figure 4.

3.1 The BETA Detector

The Big Electron Telescope Array (BETA) shown in Figure 5 is based upon a 194 msr electromagnetic calorimeter instrumented with gas Čerenkov and Lucite Čerenkov detectors for clean electron identification with a $\pi^{\pm}$ rejection of at least 1000:1. BETA's low sensitivity to backgrounds, high pixelization, low channel deadtime, and large solid angle with adequate electron energy resolution make it ideal for large x measurements in the DIS regime. A

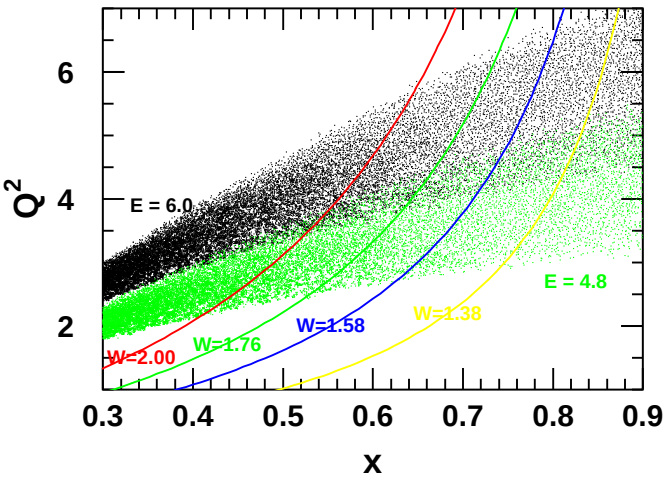

Figure 3: Kinematic region covered by the BETA detector system for 4.8 GeV (green) and 6 GeV (black) beam energy, with a central angle of 40°. Also shown are the lower W limits of the second and third resonance region, the transition region and DIS.

drift space between the Lucite Čerenkov and the Calorimeter make BETA a telescope with sufficient pointing accuracy to isolate events well within the scattering chamber.

The calorimeter portion of BETA will be that used for the upcoming G_E^p/G_M^p measurement, augmented with additional magnetic shielding. Much of the infrastructure for the G_E^p/G_M^p calorimeter (e.g. cable runs and stand) can be used for SANE, and we hope there will be a large overlap between the two collaborations. If this proposal is approved, Hall C engineering staff will design the calorimeter infrastructure with enough flexibility to accommodate both experiments where possible. The Lucite Čerenkov and the gas Čerenkov will be new construction. A detailed list of BETA parameters is given in Table 1.

Table 2 contains a list of the reconstruction resolutions. The reconstruction resolutions in Table 2 differ from the tracking resolutions of Table 1. The tracking will be used to identify events coming from the area of the coils, as opposed to the target chamber walls for example. Once the tracking isolates the events to approximately the target cell, the track will be reconstructed assuming that it originates in the target cell. This assumption is very good based on experience from G_{En}.

The reconstructed angular resolution is a combination of the resolution of the centroid determined in the calorimeter and the distortion of the particles trajectory through the target magnetic field. The former contribution is independent of momentum and is small, about 2 mrad. The later is dependent on the momentum and ranges from large to small, about 17 mrad to 2 mrad.

3.1.1 The Gas Čerenkov

The principle requirements for the first detector element are to provide high efficiency for electron detection while maintaining a pion rejection factor of at least 1,000:1. A gas Čerenkov

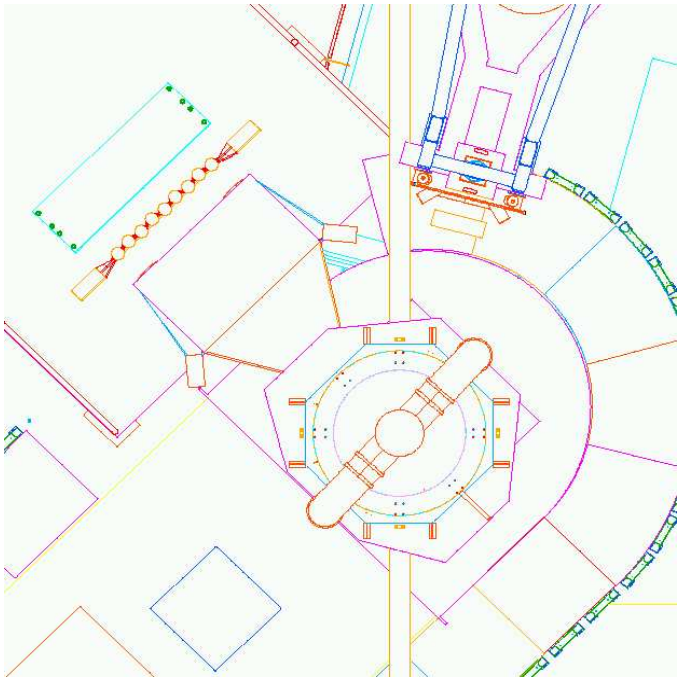

Figure 4: Plan view of the experimental setup with beam entering from the right. The UVa polarized proton target is located in the center, the BETA detector is in the upper left and HMS first quadrupole is in the upper right.

is the logical technology choice because the low areal density minimizes the probability of δ-rays from $\pi + e$ scattering. The Gas Čerenkov design will be discussed in more detail here than the other BETA components because a good design is critical for the experiment.

Firstly, operation at atmospheric pressure is assumed in order to simplify the mechanical design and minimize the window thickness. The choice of radiator gas is a complex trade-off between many parameters of which we are well aware. The reference design presented here assumes the use of dry N_2 gas. At 20° C, the index of refraction n of N_2 is approximately 1.000279, yielding a β threshold for Čerenkov light emission by pions of

$$\beta_{threshold} = \frac{1}{n} = 0.999721,$$

which corresponds to a momentum threshold for pions of 5.9 GeV/c. Pions above this momentum threshold should be extremely rare with 6 GeV beam and would be removed in any case with our software electron definition, >3-5 photoelectrons. This cut will also suppress low energy δ rays and virtually extinguish expected scintillation backgrounds from all non-electron charged particle species. Desiccants will be emplaced in the radiator box, it will be flushed with dry N_2 to remove contaminants, and then hermetically sealed with a slight overpressure (1 cm of water equivalent). A thin front window of Tedlar will provide a light-tight seal. An interior polymer window will provide a gas-tight seal capable of withstanding normally variations in barometric pressure (± 1" of water equivalent).

Eight roughly 50 cm by 70 cm mirrors, arranged in two overlapping columns of 4 mirrors, will be required to cover the rather large acceptance which has a vertical/horizontal aspect

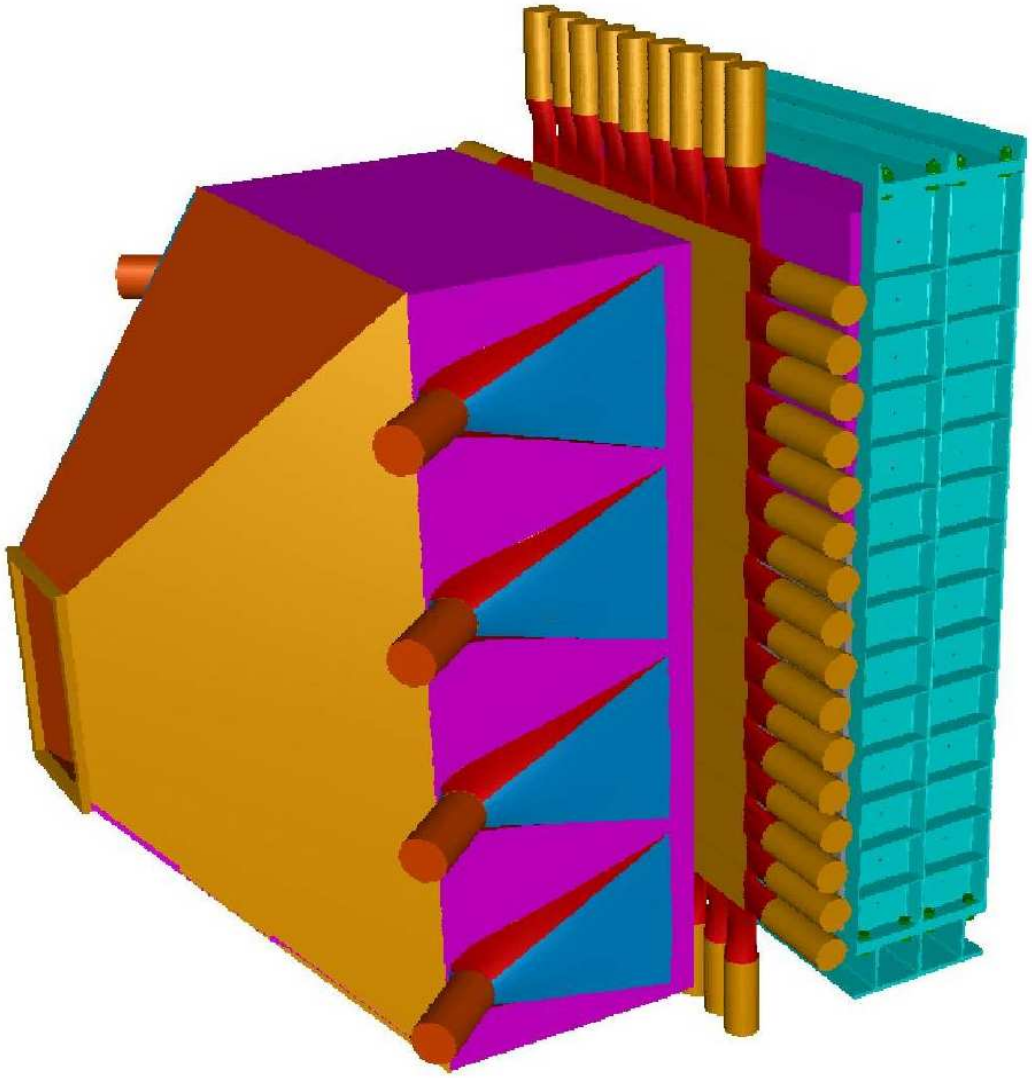

Figure 5: The BETA detector with its gas Čerenkov, Lucite Čerenkov, and calorimeter sections.

Table 1: Basic parameters of the BETA detector. The "distance" is the 50 cm radius of the scattering chamber plus the running length of the detector. The first element of BETA begins immediately outside the Aluminum vacuum window of the scattering chamber. The solid angle calculation assumes an effective calorimeter length of 20 cm, or an effective calorimeter distance of 345 cm.

BETA Component:	Length (cm)	Distance (cm)
Gas Čerenkov (GC)	175.	225.
GC radiator gas	125.	
GC mirrors (at 45°)	50.	
Lucite Čerenkov (LC)	3.75	240.
Drift (D) Length	85.	325.
Calorimeter (CAL)	40.	365.
BETA Solid Angle:		
Calorimeter Frontal Area	218 (V) x 120 (H)	
Naive Solid angle	219 mSr	
Solid angle with fiducial cut	194 msr	
BETA Resolutions:		
Electron Energy Resolution	$5\%/\sqrt{E(GeV)}$	
Assuming 3.6 cm (RMS) at LC:		
Angle Resolution	2.0° (RMS)	
Vertex Resolution	9.9 cm (RMS)	

ratio of roughly 2:1. Mirror backings will be cut to the desired ellipsoidal shape from a Rohacell-carbon fiber composite on a computerized milling machine, thin glass sheets will be oven-slumped into glass forms with the same shape, the thin mirrors will be sent to a vendor for proprietary coating with high UV reflectivity[2], and the coated mirrors will finally be glued into their Rohacell beds using a zero-shrink glue.[33] Glass mirrors are preferred over plastic for their long term stability: they should maintain their curvature without creep and are insusceptible to crazing. Pending a detailed optical ray-trace analysis, it appears that the radiator is short enough to focus all Čerenkov photons onto a baffled 5"photocathode, such as the Photonis XP4508B, without the use of a Winston cone.

The electrons of interest are above 0.7 GeV/c and are deflected by the target field less than a few degrees. Thus, to an excellent approximation, the mirrors can be designed for point-to-point focusing from the target cell to the photomultiplier photocathodes. This permits the two towers of mirrors to be optimally aligned with a small, bright light bulb located at the same target-mirror distance. This geometry also permits good rejection of stray light from scintillation and low energy δ rays (which are preferentially emitted at angles several times larger than the Čerenkov cone).

[2]The coating is aluminum with a passivating and UV-extending layer of MgF_2, but quality control is critical to the ultimate performance.

Table 2: Resolutions of SANE for $E = 4.8$ and 6.0 GeV and $\theta_{central} = 40°$. The momenta shown roughly correspond to the lowest and highest x for DIS and the highest x for the second resonance region.

E' (GeV)	x	W (GeV)	$\delta\theta$ (mrad)	$\delta E'$ (GeV)	δx	δQ^2 (GeV^2/c^2)	δW (GeV)
			$E = 6.0$ GeV				
1.0	0.30	2.73	10.1	0.050	0.024	0.160	0.045
1.7	0.59	2.04	4.5	0.065	0.035	0.196	0.076
2.2	0.87	1.35	2.9	0.074	0.048	0.214	0.130
			$E = 4.8$ GeV				
0.8	0.24	2.57	17.0	0.045	0.028	0.131	0.039
1.4	0.49	2.03	5.9	0.059	0.034	0.143	0.061
1.9	0.78	1.43	3.9	0.069	0.050	0.162	0.100

Number of photoelectrons for the N_2 gas Čerenkov

The number of Čerenkov photons emitted per cm per nm for N_2 gas at 20° C assuming a constant index of refraction of n = 1.000279 is

$$\frac{dN}{d\lambda} = \frac{2\pi z^2 \alpha}{\lambda^2}(1 - \frac{1}{\beta^2 n^2})$$

and is plotted for highly relativistic electrons in Figure 6. In the same figure are smaller magnitude curves which take into account the quantum efficiency of a vendor's bi-alkali photocathode for 3 different window types. Integrating these curves using a realistic lower cutoff of 200 nm, one estimates the number of photoelectrons per cm of gas traversed. (See the second column of Table 3.) For our reference design radiator gas thickness of 125 cm, assuming a mirror reflectivity of 90% and only 90% transmission through the gas-window interface due to Fresnel reflection, we can expect 17-20 photoelectrons depending on whether UV Glass or Quartz windows are used. (See the final column of Table 3.) With either window, the photomultiplier tubes will be hermetically isolated from the often Helium-rich environment near the target platform.

The fact that the increase in photoelectrons is only 18% when Quartz rather than UV glass is used is due to our conservative 200 nm minimum wavelength cutoff. If we succeed in procuring mirror coatings with excellent reflectivity down to 175 nm, where the bi-alkali photocathode response begins to drop off rapidly, the improvement over UV Glass would potentially rise to nearly 40% (i.e., 24.7 photoelectrons for Quartz windows). Since this is roughly twice the number of photoelectrons required by our application, we may be able to shorten the gas radiator and improve the pion rejection even further. However, O_2 and H_2O contamination must be limited to about 100-200 ppm for operation below 200 nm; if diffusion of O_2 through the large front plastic window is a limiting factor, then a continuous flow of N_2 could be employed.

In conclusion, a reasonable estimate suggests that we can expect 17-20 photoelectrons

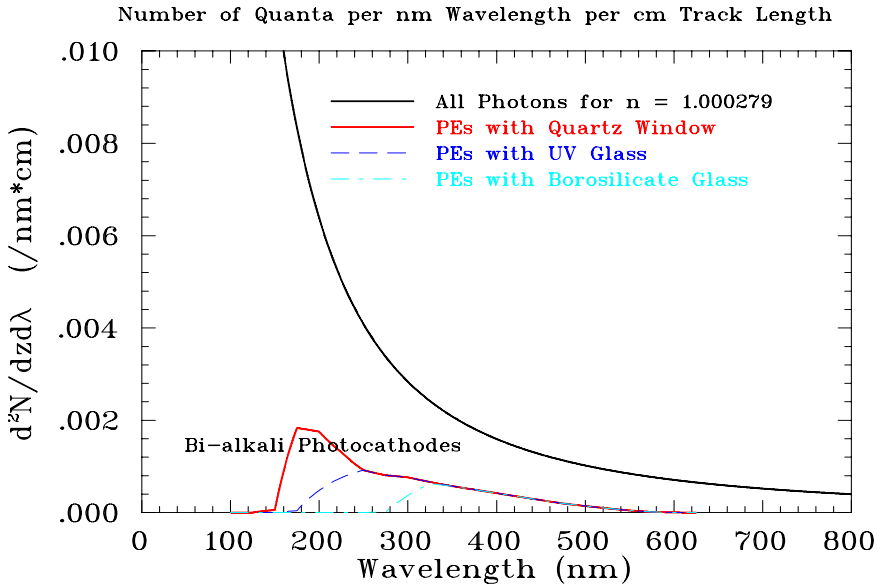

Figure 6: The number of Čerenkov photons emitted per nm per cm of N_2. Also shown is the effect of a bi-alkali photocathode with different windows. The integral of the efficiency-weighted curves gives dN/dz, the number of photoelectrons per cm of gas. Numerical results are summarized in Table 3.

for a Čerenkov with a 125 cm N_2 gas radiator.

Table 3: Expected number of photoelectrons for a 125 cm N_2 radiator assuming photomultiplier tubes with bi-alkali photocathodes. The finite reflectivity of the mirror (90%) and Fresnel reflection at the gas-quartz interface (10%) have been taken into account in the last column.

Window	dN/dz (cm^{-1}) (200nm - 650nm)	Naive total pe's	Actual total pe's (including mirror, Fresnel)
Quartz	0.199	24.9	20.2
UV Glass	0.169	21.1	17.1
Borosilicate Glass	0.0908	11.4	9.2

Pion rejection

The probability for a pion to produce a δ ray above Čerenkov threshold is shown in Figure 7 for a realistic window and radiator configuration. At about $T_\pi = 0.5$ GeV, it becomes possible for a pion to scatter an electron above Čerenkov threshold, however the probability does not reach 0.01% until about $T_\pi = 0.75$. It is clear from the figure that for a large range of pion energies, a N_2 radiator meets our requirement for 1000:1 charged pion rejection. Low energy, relatively large angle δ rays dominate the knock-on probability. These events produce few photoelectrons because they are barely above Čerenkov threshold. (Figure 8) A tight, baffled focusing arrangement for the Čerenkov photons, combined with

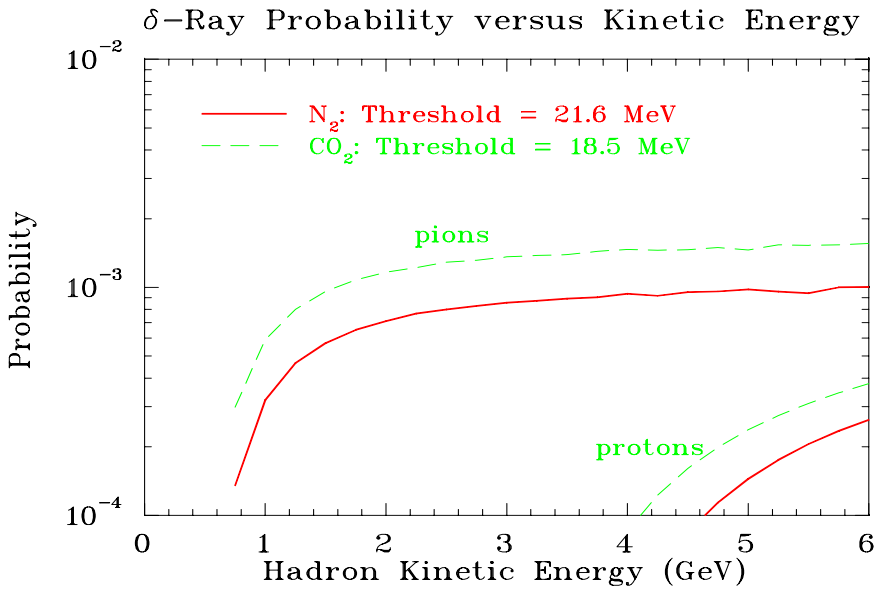

Figure 7: The pion and proton knock-on probabilities versus hadron kinetic energy for N_2 and CO_2 radiators. The calculation takes into account the 16 mil aluminum exit window of the target vacuum chamber, the 5 mil front window of the GC, and the 125 cm of radiator gas.

an aggressive electron definition cut (3-5 photoelectrons) will improve our pion rejection further. However, 1000:1 rejection is adequate for SANE.

A similar calculation was done for proton knock-ons and is also shown in Figure 7. The knock-on probability for protons is negligible. It is harder for the much more massive proton to transfer enough energy to an electron to cross Čerenkov threshold.

An alternative radiator gas

While nitrogen gas appears to be a near-optimal radiator for our application, it does have a weak scintillation yield which is relatively larger than other common radiator gases. This is not normally a problem since the emission is isotropic; the effects of scintillation are further reduced by the tight mirror focus, baffling, and black-painted walls. However, in the presence of very large charged particle backgrounds, this small scintillation yield can produce significant DC background in the gas Čerenkov signal.[34]

We do not believe our charged particle backgrounds will be pathological. For the particles coming from the target, the rate of the high energy ones can estimated and the low energy ones are cut off below 180 MeV/c due to the target magnetic field. For background originating downstream of the target, there will be nothing but a Helium bag to intercept the spray of particles coming from the target. A 2" lead wall will shield BETA from this potential source of background. Nevertheless, the N_2 radiator gas could be replaced with CO_2 gas in a few hours without the need to realign the mirrors. This change would reduce scintillation and increase the number of photoelectrons, but worsen pion rejection.

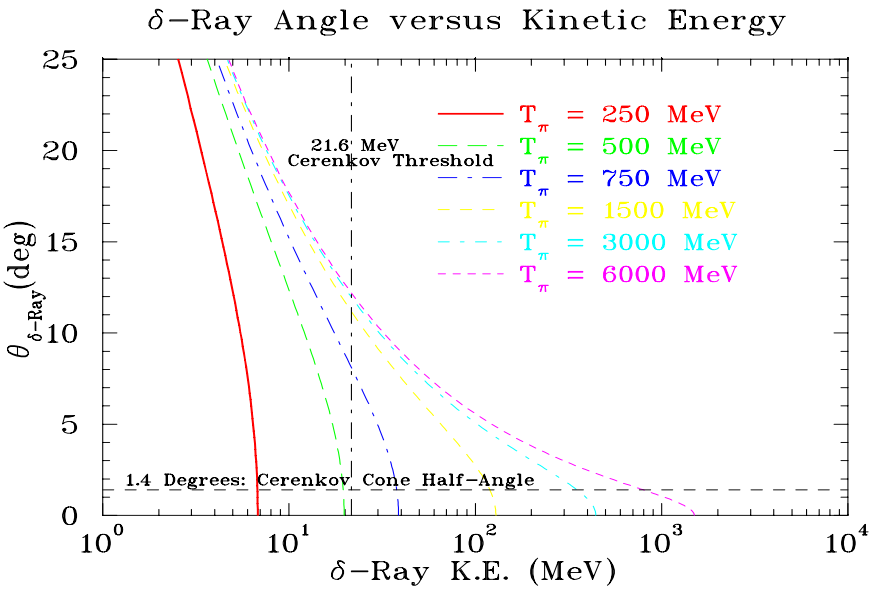

Figure 8: δ-ray angle versus its kinetic energy. Low energy, relatively large angle δ rays dominate the knock-on probability. These events produce few photoelectrons because they are barely above Čerenkov threshold.

3.1.2 The Lucite Čerenkov Hodoscope

The purpose of the second element of BETA is to provide redundant and efficient electron detection with sufficient position resolution to support limited tracking resolution. The simplest and most robust technology choice appears to be a solid, X-Y Čerenkov hodoscope. For our reference design, we assume rectangular solid Lucite radiators: 16 X-like elements and 8 Y-like elements, with the dimensions given in the Table 4.[3] Localization of an event to a given square 12.5cm x 12.5cm (X,Y) pixel implies an RMS resolution at the Lucite Čerenkov in both x and y of $12.5\text{cm}/\sqrt{12} = 3.6$ cm.

Table 4: Dimensions of the Lucite Čerenkov radiators. The longer Y-bars are twice as thick to obtain roughly the same number of photoelectrons.

Type	Thickness (cm)	Horizontal Dimension (cm)	Vertical Dimension (cm)	Quantity
X	1.25	80.	12.5	16 bars (32 pmt's)
Y	2.5	12.5	160.	8 bars (16 pmt's)
			Total:	24 bars (48 pmt's)

Lucite has an index of refraction n of 1.49 and therefore a relatively low β threshold of

$$\beta_{threshold} = 1/n = 0.671$$

[3]Wire chambers would be inoperable and scintillating hodoscope performance would be severely compromised by the large, low energy γ background seen by the forward scintillator veto array in the Hall C G_E^n experiment which used the same UVa polarized target and luminosity as proposed here.

Compared to scintillator, it is very insensitive to charged particles below the β threshold as well as to neutrons and γ rays. But Lucite is equally sensitive to electrons and relativistic pions with pions dominating the total rate.

In reference [35], a Lucite Čerenkov was operated in total internal reflection (TIR) mode to assist in kaon/proton separation. This means that the Čerenkov cone angle

$$\theta_{cerenkov} = \arccos 1/\beta n = 47.8^{\circ},$$

was greater than the critical angle for TIR

$$\theta_{critical} = \arcsin 1/n = 42.2^{\circ},$$

assuming normal incidence. The bars were wrapped with light-absorbing material to absorb any Čerenkov light emitted by slower backgrounds at angles below the critical angle for TIR. In our application, the range of incident angles is generally too large to count on TIR to propagate light to both ends of a radiator bar (although it will work for the central region), so a typical event will have a good signal at only one end. Wrapping the bars in reflective material will increase the overall light collection as well as the light yield at the unfavored PMT. The longer Y-bars must be thicker than the shorter X-bars in order to obtain the same number of photoelectrons. A reasonable estimate of the photoelectron yield, based on the performance of the 2.5 cm thick, 40 cm long bars in [35], is that our somewhat longer, but reflectively wrapped bars will yield 10 pe's at the favored PMT. The total radiation length of Lucite is 11% which will not significantly deteriorate the calorimeter energy resolution.

3.1.3 Electromagnetic Calorimeter

The electromagnetic calorimeter consists of a stack of optically isolated lead-glass blocks utilized in fly's-eye mode. Individual blocks are either 40 cm or 45 cm in length, and are approximately 4 cm x 4 cm in cross section. The stack is 218 cm high by 120 cm in width or, in terms of blocks, 56 blocks high by 30/32[4] blocks wide for a total of 1744 blocks. The block size is well-matched to the Moliere radius, so we expect our fiducial volume to consist of nearly the entire array except for the outermost layer of blocks. Very thin dead layers (of order 1 mil) separate the blocks. The hit position will be determined by the energy-weighted centroid of the blocks which share energy in a cluster, and is $\leq$ 0.5 cm. This position uncertainty is of the same scale as the RMS position uncertainty of the target vertex, so the total RMS angle uncertainty is only several mrad. The electron energy resolution is assumed to be $5\%/\sqrt{E(GeV)}$ which is certainly reasonable for fly's-eye mode.

Pulse pile-up can change the measured energy of an electron. Two factors make pile-up in BETA surprisingly small. First, BETA can be divided into many smaller detectors, each of is large enough to contain the shower. Second, the rate of events with significant energy in the calorimeter is quite low.

We have studied the impact of pulse pileup in our simulations. We recorded the amount and rate of energy deposited in a fixed 3 x 3 group of blocks in the calorimeter. We excluded events in which we found a "seed" block, one with more than 350 MeV visible energy,

[4] 30 wide for the 40 cm blocks, 32 wide for the 45 cm blocks.

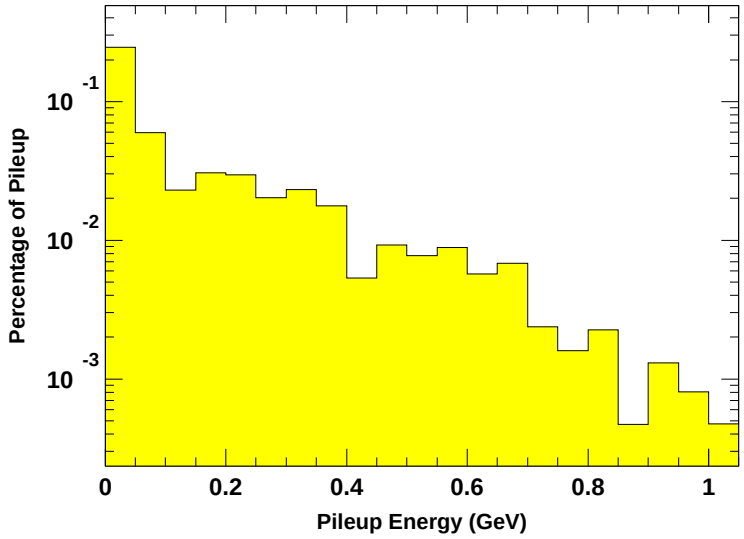

Figure 9: Percentage of pileup in a 3 x 3 group of blocks in the calorimeter as a function of the pileup energy. We assume a 100 ns ADC gate in determining the percentage.

immediately outside of these nine blocks. The simulation would identify such a block as the center of a new cluster. We can ignore this new cluster, because if we reconstructed a cluster centered in the fixed group of nine and one immediately outside of those nine blocks, then we would identify this event as a double cluster event which would be excluded from electron analysis.

The results of this pileup study are shown in Fig. 9. This figure shows the percentage of a pileup with an electron event, assuming a 100 ns gate, as a function of the pileup energy, the energy that would be added to an otherwise good event. The total probability for pileup is about 0.5% of which about one-half is with a pileup energy of less than 50 MeV. We found that there was no significant variation in the pileup depending on the location of the fixed group of nine blocks within the calorimeter. We conclude that pileup is an entirely tractable issue.

The downside to the small size of the blocks is that, since they are individually instrumented with photomultiplier tubes, a considerable number of channels of HV, fast electronics, cabling, and patch-panel infrastructure need to be supplied. This effort is underway by a combination of the G_E^p/G_M^p collaboration, Halls A and C, and via loans of digitizing electronics from Fermilab. SANE will require an ADC per block. Having a TDC per block would be welcomed but is not required.

3.1.4 BETA Calibration

Calibration for the gas Čerenkov and the Lucite Čerenkov in terms of photoelectrons can be done quickly with the single photoelectron response provided the photomultiplier tubes

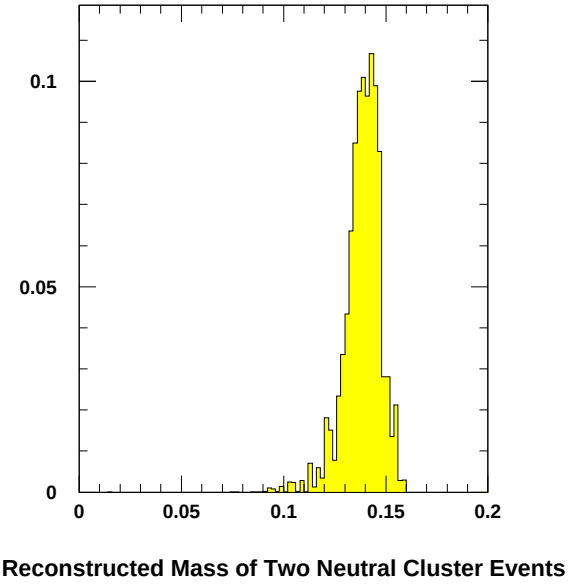

Figure 10: Histogram of the mass spectrum reconstructed from two neutral cluster events as performed by the simulations.

have good single photoelectron resolution. Using cosmic ray muons, only approximate gains for the calorimeter can be determined because it doesn't appear practical to tip it to point near the zenith.

Calorimeter calibration will be performed via π^0 mass reconstruction and $e+p$ elastics. The π^0 reconstruction approach has been utilized in other calorimeter-based experiments such as RadPhi (E94-016) at JLab[36] and E852 at Brookhaven [37]. The $e+p$ elastics will be performed once as a check on the π^0 calibration.

The π^0 reconstruction is performed by examining mass spectrum of two photon events. A global fit varying the energy calibration of the blocks is performed to a sample of neutral two cluster events in the calorimeter (these events are nominally two photon events) to minimize the mass spectrum. Experiment E582, which has a fairly similar experiment setup as SANE, was able to get a π^0 mass resolution of 10 MeV. One advantage of this approach is that the data can be collected simultaneously with the production data so that rate dependent issues are automatically addressed. The $e+p$ calibrations provide a cross check on the γ versus e^- response in the lead glass.

Figure 10 is a plot of the mass spectrum reconstructed from two neutral clusters in the GEANT simulations of SANE. The peak is clearly dominated by two photon events which originated from a π^0. The simulation included the effects of reconstructed cluster energy and position resolution. One convenience of using $\pi^0 \rightarrow \gamma + \gamma$ events is that they are entirely neutral, i.e. trajectories are not impacted by the target field.

For $e+p$ elastic scattering calibration, the HMS will be used in coincidence to define electrons of known energy in the calorimeter. As this is a check of the π^0 calibration, it can be performed over a subset of the calorimeter, which reduces the need to move BETA

between calibration and production.

One possible set of kinematics for the gain calibration is with 2.4 GeV beam energy. With BETA at 40° and its nominal drift and the HMS at 37.7°, about 5% (70 blocks) of the calorimeter would detect electrons that in coincidence with protons in the HMS. In this configuration, the target coils could remain oriented along the beam line. As the target material will not be polarized, it will be possible to increase the beam current to 1 μA to increase the counting rate.

Gain Monitoring

Gain monitoring of the calorimeter will be carried out using a primary system checked by at least one other technique.

The primary gain monitoring system will be similar to the successful design used at BNL for a 3000-element lead-glass electromagnetic calorimeter.[37] A 1 cm thick Lucite sheet will be weakly optically coupled to the front of the calorimeter blocks by a small air-gap. In a nearby enclosure, a laser will excite a piece of scintillator whose light will be brought to all four edges of the sheet by 1mm diameter quartz optical fibers. The amplitude of the laser and scintillator response will be monitored using a stable optical power splitter and a PIN diode in a temperature-controlled environment. The light should in principle be trapped by total internal reflection, but in reality is able to leave the sheet by a combination of Rayleigh scattering and scattering from surface imperfections. Although a uniform distribution of the light to the blocks is more of a convenience than a requirement, the uniformity of the light distribution is expected to be better than 10%. The light levels can be adjusted to approximate typical electron energy depositions: using 400 μJ pulses from the laser, the BNL collaboration was able to deposit the equivalent of 7 GeV of light in each block. The advantage of this technique over running a separate fiber to each lead-glass block is a greatly reduced cost in dollars, installation time, and maintenance. The proposed system should also be much more reliable with essentially no drop-outs unless a photomultiplier tube malfunctions. The only disadvantage is the additional 0.029 of a radiation length of material in front of the calorimeter. The BNL collaboration searched for cross-talk between lead-glass blocks (due to light exiting the front face of one block, reflecting from the Lucite sheet, and scattering into another block) but found no evidence for it at their level of sensitivity.

Although our primary gain monitoring system will have significant redundancy, an independent check would be valuable. The simplest possible alternative would employ the significant ($\simeq 1/3$) fraction of high energy pions which pass through the calorimeter without undergoing hadronic interactions. These pions leave a small, distinctive Čerenkov signal which appears as a peak in an energy spectrum, see Figure 11. Such events are already routinely used to help gain-match the lead-glass blocks in the HMS calorimeter. A clean pion punch-through trigger could be formed by a (prescaled) coincidence between the LC, the calorimeter with a low energy threshold, and scintillator paddles located behind the calorimeter.

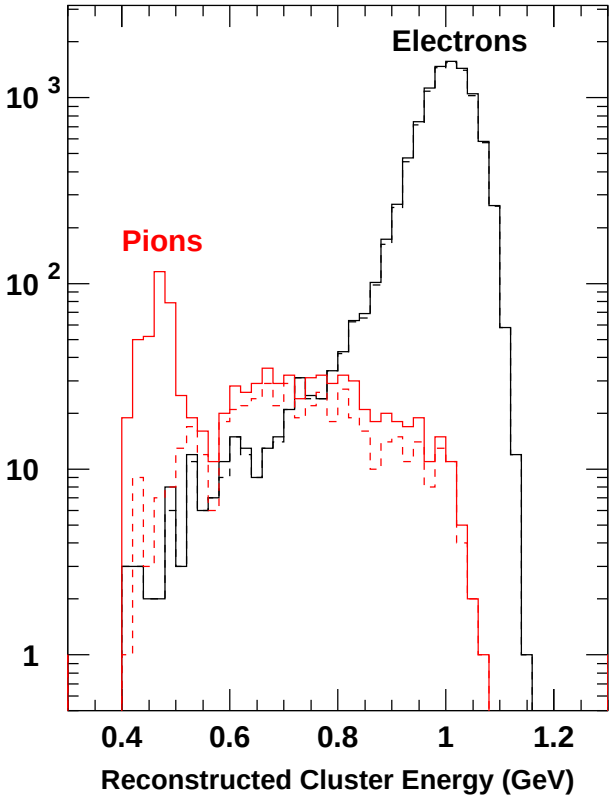

Figure 11: Reconstructed energies for 10,000 electrons and pions with a momentum of 1 GeV/c thrown at the center of BETA. The reconstruction requirement of a calorimeter block with at least 350 MeV of visible light reduces the pions by a factor of 9. The dashed histograms are the events that survive a maximum energy deposited in veto wall behind the calorimeter. The veto wall essentially eliminates the minimum ionizing peak from pions.

3.2 Target

In this experiment we will use the U. of Virginia polarized target, which has been successfully used in E143/E155/E155x at SLAC and E93-026 and E01-006 at JLab. This target operates on the principle of Dynamic Nuclear Polarization, to enhance the low temperature (1 K), high magnetic field (5 T) polarization of solid materials (ammonia, lithium hydrides) by microwave pumping. The polarized target assembly contains two 3–cm–long target cells that can be selected individually by remote control to be located in the uniform field region of a superconducting Helmholtz pair. The permeable target cells are immersed in a vessel filled with liquid He and maintained at 1 K by use of a high power evaporation refrigerator.

The coils have a 50° conical shaped aperture along the axis and a 34° wedge shaped aperture along the vertically oriented midplane.

The material during the experiment will be exposed to 140 GHz microwaves to drive the hyperfine transition which aligns the nucleon spins. The DNP technique produces proton polarizations of up to 95% in the NH_3 target. The heating of the target by the beam causes a

drop of a few percent in the polarization. The polarization slowly decreases due to radiation damage. Most of the radiation damage is repaired by annealing the target at about 80 K, until the accumulated dose reaches $> 2 \times 10^{17}$ electrons, at which the material needs to be changed. The luminosity of the polarized material in the uniform field region was 85×10^{33} cm^{-2} Hz.

As part of the program to minimize the sources of systematic errors, the target polarization direction will be reversed after each anneal by adjusting the microwave frequency.

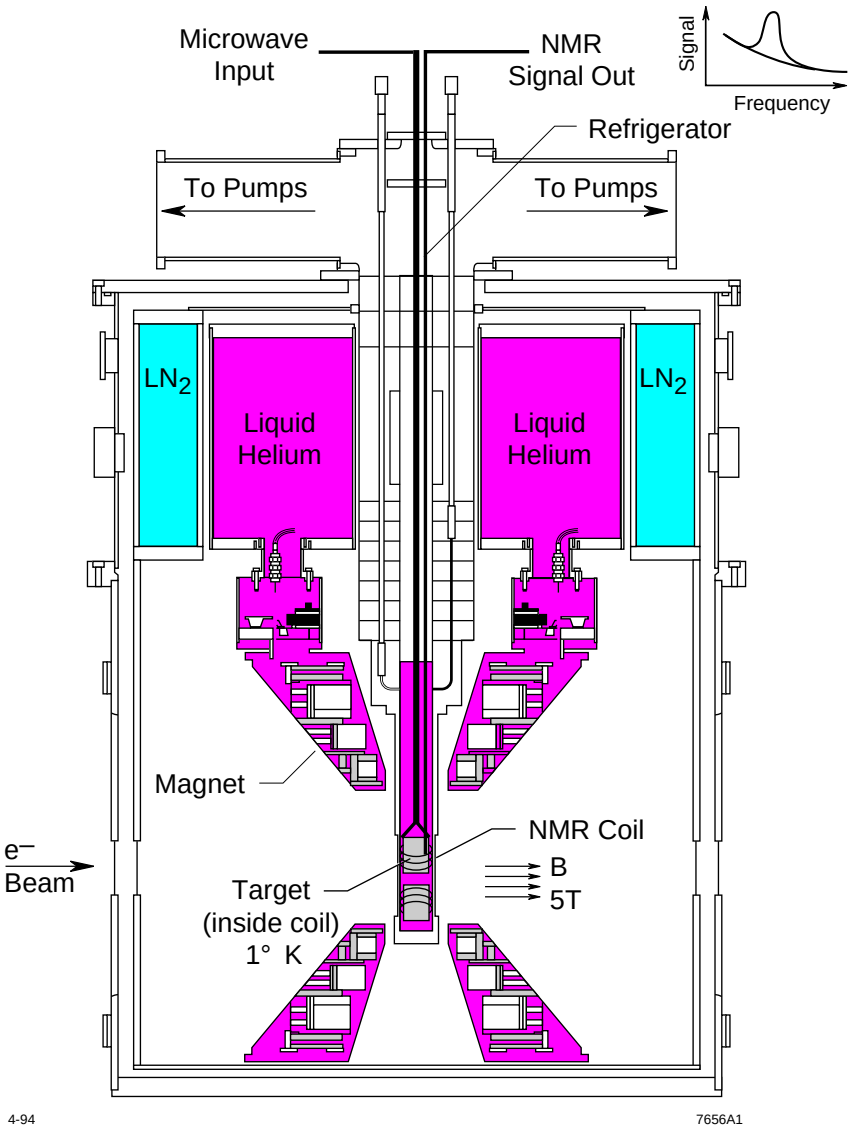

Figure 12: Cross section view of the polarized target

3.3 HMS

The High Momentum Spectrometer (HMS) plays an essential role in the experiment because, while BETA can distinguish between charged and neutral particles, it is blind to the *sign* of

the charge. Hence the measurement of charge-symmetric backgrounds (i.e., electrons arising from e^+e^- pairs), which is particularly large at smaller x, will be carried out in parallel using the HMS. The mm-level Y_{target} reconstruction of the HMS will also be useful to make sure that no significant beam halo is clipping the inner edges of the Helmholtz coils.

3.4 Rates in Detector

The data rates from BETA will be manageable because of two high thresholds. First, particles must have momentum greater than 0.18 GeV/c to pass from the target through the target field to BETA. Second, we will require a threshold of at least 0.5 GeV in the calorimeter. A list of the estimated particle and trigger rates in BETA are shown in Table 5. The rates similar for all kinematic settings.

We estimated the rates in the gas Čerenkov assuming the 0.18 GeV/c momentum threshold. We examined the rates for electrons, positrons and charged pions. We assumed that neutral pions which pair produce are described by the positron rates. The probability of nucleons firing the gas Čerenkov is so low that they can be safely ignored. The gas Čerenkov trigger rate was calculated assuming 100% efficiency for electrons and positrons and a 100:1 online pion rejection. The gas Čerenkov trigger rate is dominated by charged pions. To lower the trigger rate, we could increase the Čerenkov threshold with a cost of negligible loss of electrons.

The signal rate in the gas Čerenkov is not an issue. At worst, the PMTs will see about 1KHz of events coming from the target. As the mirrors are designed for point-to-point focusing from the target to the PMTs, background particles coming from locations other than the target will have a very low efficiency.

The rates of particles in the calorimeter take into account the visible energy deposited in the calorimeter (as discussed in more detail in Section 4). We applied a threshold of 0.5 GeV for the total visible energy in the calorimeter. The neutral pions heavily dominate the calorimeter rates.

The primary trigger will be formed by a coincidence of the gas Čerenkov with a 0.5-1 photo-electron threshold and the calorimeter with an energy dependent threshold. We list the predicted true and accidental coincidence rates for this trigger in Table 5. The true coincidence rate is the sum of the electron and positron rate and the charged pion rate divided by 100 to account for the Čerenkov rejection. The other particles do not trigger the Čerenkov. The accidental coincidences are calculated assuming a 200 ns time window. The highest rate is approximately 500 Hz, which is well below the limit of the data acquisition system.

The accidental rates between the detectors will be further reduced in off-line analysis. An offline rejection of 1000:1 will reduce the accidentals a factor of 10. In addition, if we assume that a track through the gas Čerenkov fires two of the eight PMTs, then spatial correlations between the calorimeter position and the gas Čerenkov will reduce the accidentals another factor of 4. Thus, we will be able to trivially reduce the offline accidental coincidences between detector elements to below 1%.

We will form several triggers. In addition to the primary trigger of the gas Čerenkov in coincidence with the calorimeter, we will form prescaled triggers of various combinations of

Table 5: List of predicted particle rates passing through the gas Čerenkov and in the calorimeter, as well as the overall BETA rates. All rates are in kHz. "Trig" indicates trigger rates for that detector and includes the online sensitivity of the detector in question. See text for further description.

		Gas Čerenkov			Calorimeter				BETA	
E	θ_N	e^-+e^+	$\pi^++\pi^-$	Trig	e^-+e^+	$\pi^++\pi^-$	π^0+p+n	Trig	True	Accd
4.8	-180	0.6	242	3.0	0.3	9.6	72.1	82.1	0.39	0.05
4.8	-80	1.0	223	3.2	0.3	10.4	70.6	81.3	0.39	0.05
6	-180	0.8	255	3.4	0.3	10.7	81.4	92.4	0.41	0.06
6	-80	1.2	236	3.6	0.3	11.5	79.8	91.6	0.39	0.07

the gas Čerenkov, Lucite Čerenkov and calorimeter for diagnostic purposes. The rate of the sum of all triggers will be held well below the 2kHz limitations of the current DAQ system.

3.5 Beam Line

The beam line requirements for SANE are the same as those of the 2001-2002 running of G_{En} and the Resonance Spin Structure experiment (RSS). We will use the Hall C Moller polarimeter in its standard configuration to measure the beam polarization. The beam line instrumentation will need to work with beam currents as low as 50 nA. The two upstream chicane magnets will be necessary for the non-parallel target field measurements. A large, slow raster uniformly distributed over the surface of the target cell is critical to the performance of the target. We also need the the Secondary Emission Monitor to determine the beam position. Downstream of the target, we will use a helium bag and a low current dump in the hall for the non-parallel field measurements. The special dump is necessary because the non-parallel target field will deflect the beam away from the normal Hall C dump.

4 Detector Response

Pb-glass calorimeters are excellent tools for examining electromagnetic physics which do not require high momentum resolution. They provide the possibility of large angular acceptances coupled with excellent detector position resolution when the block sizes are adequately small.

The SANE approach is to 1) take advantage of the properties of the target to reduce background and 2) incorporate excellent PID into BETA. To understand the response of BETA to the experimental setup, it is important to understand the effects of the target coils and magnetic field, the rates of the various particles, and the detectors response to those particles. Each of those elements will be discussed below.

4.1 Target Magnetic Field

The 5 T target field coupled with the target magnetic coils has a number of interesting effects on the acceptance of the experiment. Fig. 13 offers of visual summary of these effects. These

effects include a momentum threshold for particles, a distortion of the accepted phase space at low momentums, and a small rotation of the phase space at higher momentums. The Monte Carlo simulation of the acceptance used to generate this figure included the extended target size, the large raster radius, the geometry of the magnet coils, the target field and the detector location and geometry.

Low energy charged particles will be captured by the solenoidal target magnetic field and swept into the direction of the target field. For the target field orientations, the momentum threshold at which particles can escape the field is 0.18 GeV/c. This sweeping action will reduce the direct contributions from the low energy particles generated in the target. This threshold is clearly seen in the lower plots of Fig. 13.

Just above this momentum threshold, particles from large out-of-plane angles are steered through the magnet coils by the target field. In contrast, the scattering angles are not significantly distorted at low momentums. The scattering angle acceptance is approximately what one would expect considering the geometry of the coils and the length along the beam of the target cell.

The dependence of the angular acceptance on the momentum is demonstrated in the top two graphs of Fig. 13. The acceptance for all momentums deviates from the simple geometric acceptance one expects when one ignores the target field. When we require the momentum to be greater than 0.75 GeV/c, then the acceptance is much closer to the naïve geometric acceptance. The deviation of this case from the naïve expectation is that the events are rotated slightly in ϕ_{scat}, as one would expect from a solenoid field.

4.2 Cross Sections

Unlike a magnetic spectrometer, the BETA will see everything that comes from the target and passes through the target field. This includes both positively and negatively charged particles, as well as neutrals. Thus, it is necessary to consider background rates of all possible particles.

We used various codes to calculate the inclusive rates for the various particles. For the electron rates, we used the MRST 2001 NLO code [38]. For the positrons, we used a parameterization that was based on SLAC measurements [39]. The charged pions were calculated from the WISER code, and the neutral pions were based on the same code, but were twice the sum of the charged pion rates. Proton and neutron rates were calculated using the Lightbody and O'Connell code EPC [40]. We also used the WISER code to calculate the charged kaon rates, but found the contributions to be small enough to ignore. Results from each of these codes have been checked against measurements and all agree reasonably well with one exception, positrons.

In the past, single-arm experiments have measured positron rates and asymmetries as a means to understanding the charge-symmetric background in their measurements. The charge-symmetric background, as the name implies, comes from reactions that produce a positron-electron pair. For measurements which detect scattered electrons for the primary reaction, a measurement of the positron rate and asymmetry allows one to correct for the electron contribution from pair production to the desired primary reaction.

Two different experiments at JLab have measured the positron to electron ratio at kinematics similar to SANE. The A_1^n collaboration in Hall A performed test measurements using a

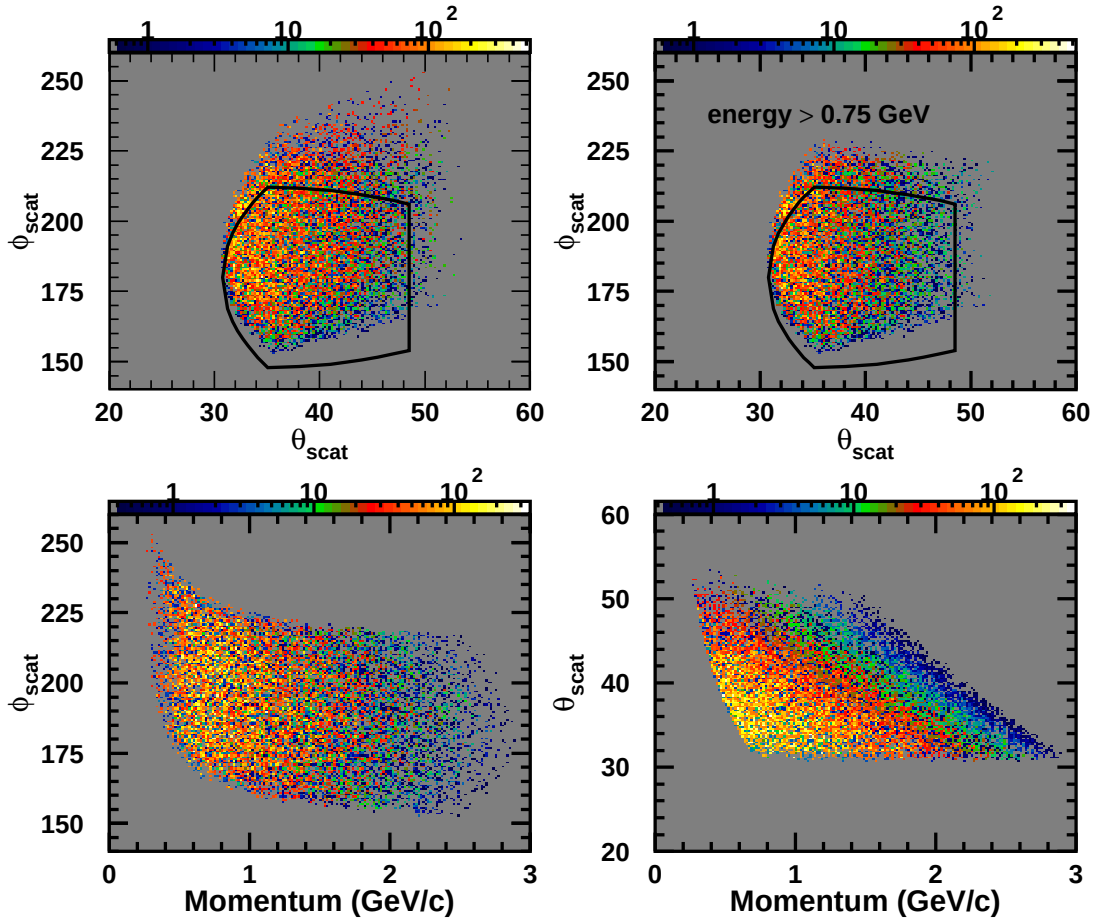

Figure 13: Plots of the electron acceptance of SANE considering the ex(tended target, the target magnet coils, the target field and the geometry of the BETA. θ_{scat} and ϕ_{scat} are the polar and azimuthal angles of the scattering at the vertex. The upper left plot is ϕ_{scat} versus θ_{scat} distribution for all momentum. The black lines denote the naïve acceptance considering the target coils, and the calorimeter acceptance and no target field. The upper right plot is the same as the upper left, but with a minimum energy of 0.75 GeV/c. The lower left and right plots are the ϕ_{scat} and θ_{scat} versus momentum, respectively. For all four graphs, the z axis represents rates in arbitrary units.

15 cm LH_2 cell, while the EG1 collaboration in Hall B has extracted the ratio from their production data. The beam energy for both measurements was approximately 5.6 GeV. For the A_1^n measurement, they measured ratios of 15.5% and 3.6% at 0.9 GeV/c and 1.5 GeV/c[41], respectively, while for EG1 the ratio is 30% and 7% at 1.0 and 1.7 GeV/c [42], respectively. From this comparison, it is clear that the e^+/e^- ratio is experimental setup dependent.

The most likely source of the high energy charge-symmetric background is π^0's. The pairs are created either from the 1.2% Dalitz decay $\pi^0 \rightarrow \gamma + e^- + e^+$ or from high energy photons from the π^0 decay passing through matter. If the primary source of the charge symmetric background is the rare decay, then the e^+/e^- ratio should be independent of the target thickness. If the source is pair production from γ's, then the amount of material between the vertex and the detector is critical. Finally, if the source is related to photo-production in the target, then the process should be related to the radiation length of the target in the beam line.

However, by any appropriate measure, the Hall A target is larger than the Hall B target. Assuming our π^0 production model for generating the charge-symmetric background is correct, there are two possible explanations for the different positron to electron ratios. The first possibility is that there is more material within CLAS on which gammas may pair produce. This additional material must be close to the target. The second possibility is that there is substantial contamination of π^+ in the positron background. Fortunately, neither of these scenarios can occur for SANE.

We use the SLAC parameterization of the e^+/e^- ratio, which agrees with the Hall B measurement at 1 GeV/c. Because the calorimeter will see both electrons and positrons, we multiply the SLAC parameterization by a factor of two. As a check, we compared through our simulations the distribution of positrons from this parameterization to that of single electron-like events when we throw π^0 events; the two distributions are in good agreement.

4.3 Pb-Glass Response

We modeled the response of the Pb-Glass calorimeter in BETA to the various particles using GEANT. While the calorimeter is an excellent device to measure electron, positron and gamma energies, it is fortunately inefficient at measuring hadron energies. Typically, only a fraction of the hadron's energy is converted into visible energy in the calorimeter. For instance, a 2 GeV π^+ incident on the calorimeter may deposit 1 GeV of visible energy in the calorimeter. If this π^+ happened to trigger the Čerenkov detectors, via a knock-on electron for instance, then this 2 GeV π^+ would be labeled as a 1 GeV electron. Understanding the distribution of visible energy deposited in the calorimeter by the hadrons is critical to understanding the response of BETA to the background.

The GEANT simulation includes many aspects of the experiment. It includes the target field, the occlusion of angles by the magnet coils and the finite size of the target. It incorporates the cross sections for the various particles mentioned in the previous section. All the materials the particles pass through from the vertex to the calorimeter are incorporated into the simulation. The generation of Čerenkov light in the gas Čerenkov as well as in the Pb-glass blocks is also treated. [5]

[5] The visible energy in the Pb-glass blocks is then simply proportional to the number of Čerenkov photons

After the GEANT simulation generates the simulated data, an analyzer passes over this data attempting to reconstruct the events. The analyzer is principally concerned with the reconstruct of the clusters of blocks in the calorimeter. The cluster searching algorithm is similar to the one used by E852 [37]. First, the analyzer searches for "seed" blocks with energy above a certain threshold, typically 350 MeV in these simulations. It then builds clusters of blocks around these seeds for blocks with energy above a lower threshold, typically 50 MeV.

The lower threshold of 50 MeV was determined through the simulation. As this threshold is raised, the detector becomes less sensitive to low energy noise. However, as this threshold is raised, the energy resolution of the reconstructed cluster worsens because some information is not included in the reconstruction. The value of 50 MeV provides a very high threshold to eliminate background and noise in the calorimeter without significantly worsening the reconstructed energy resolution.

After the analyzer reconstructs the cluster, it determines the cluster energy and position in the calorimeter. It then calculates the scattering angle correcting for bending of the target field if there was a significant signal in the gas Čerenkov detector, i.e. if the event was most likely an electron. This process is performed independently of the type of particle thrown, i.e. the reconstruction is performed the same for all types of thrown particles.

In looking at the relative response of BETA to the incident particles, we scaled the hadrons by various factors to account for the rejection of events by the Čerenkov's. We assumed that the rejection ratio was for charged pions 10^3:1, for protons 10^4:1, and for neutrons 10^5:1. We treated the π^0's differently. We assumed that any electron/positron events from π^0's are addressed by the positron rates. This assumption is supported by a study briefly discussed in Sec. 4.2.

The relative rates of events as a function of visible energy in the calorimeter are shown in Fig. 14. The dominate background is the charge-symmetric events. We have observed that the relative contribution from these events can be significantly reduced by increasing the minimum scattering energy. For instance, increasing the minimum E' from 1.0 to 1.3 GeV reduces the low x ratio by a factor of 3. Fig. 14 incorporates the $E' > 1.3$ GeV/c cut, as do the remainder of the rate estimates. Pions are the second most significant source of background, however, their contributions are so small that they can be safely ignored. The ratios of background events to electrons for the other experimental setups are similar to the one shown.

5 Background Measurements

One benefit of the high incident background rates is that it is easy to measure the background rates and asymmetries. During normal data production, we will measure the background in the HMS, with suitable choice of polarity and momentum, and in the BETA, by relaxing PID requirements using prescaled triggers. A list of possible kinematics settings for the HMS background measurements is in Table 6. Because the positron rates are much lower than the hadron rates, the background measurements are designed for the positron measurements. It will be necessary to measure both polarities for these settings, as we are interested in the

generated in the block.

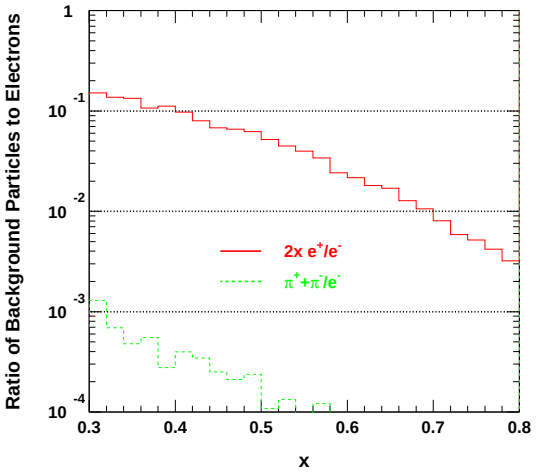

Figure 14: Ratio of background particles to electrons as a function of the reconstructed x for $\theta_N = -180^\circ$ and $E = 6$ GeV/c. The charged pion ratio have been reduced by the gas Čerenkov rejection factor. The proton and neutron ratio is not visible on this scale.

ratio of the background to electron for the rate and asymmetry. The negative polarity takes significantly less time as the electron rate is much higher than the positron rate. It will take approximately 75 hours in the parallel field target orientation to measure the positron to electron ratio in the HMS for 6.0 GeV beam so that this ratio contributes less than 1% uncertainty to the physics asymmetry.

While we will measure the positron to electron ratios in the HMS, we have multiple option of how to determine the positron asymmetry:

- The EG1b run of CLAS has copious data on the positron asymmetry.
- With the conviction that the charge symmetric processes come from photons, we can simply measure the photon asymmetry in BETA. We will have to unfold how the photon asymmetries can be expressed as charge symmetric processes in BETA, but we will need to understand this unfolding only to about 10% which is entirely reasonable for a purely electromagnetic process.
- It has been argued that the charge symmetric processes are heavily dominated by π^0 decay. We can measure the π^0 asymmetry by examining double γ events.
- We can measure the asymmetry from two "electron" events, which is the most direct means to measure the charge symmetric processes.

For the determining the uncertainties in asymmetries due to the positron background, we have used the estimated positron statistics from the EG1b run of CLAS [42].

Table 6: List of possible HMS kinematics to measure the positron background rates for 6 GeV and $\theta_N = -180°$. The e^+/e^- is the ratio of positrons from charge symmetric processes to electrons from DIS.

E' (GeV)	θ_e (°)	x	Q^2 (GeV^2/c^2)	$d\sigma(e^+)$ (nb/GeV/Sr)	e^+/e^-	rate (1/h)
1.00	36.0	0.24	2.29	0.393	1.229	2831
1.00	40.0	0.30	2.81	0.301	0.580	1336
1.00	44.0	0.36	3.37	0.225	0.261	602
1.35	36.0	0.35	3.09	0.230	0.485	1508
1.35	40.0	0.43	3.79	0.156	0.167	520
1.35	44.0	0.52	4.54	0.103	0.050	157
1.70	36.0	0.48	3.89	0.124	0.145	568
1.70	40.0	0.59	4.77	0.073	0.030	119
1.70	44.0	0.71	5.72	0.041	0.004	17

6 Systematic Uncertainties

The systematic uncertainties can be divided into two groups; those independent and those dependent on x. A summary of the estimated systematic uncertainties is listed in Table 7.

Two of the x independent uncertainties are the beam and target polarization. The Hall C Moller polarimeter is routinely run with relative uncertainties of 1% in the beam polarization. From our extensive experience with the NH_3 target, a 2.5% relative uncertainty in the target polarization is achievable.

The first x dependent uncertainty is the nitrogen contribution to the asymmetry. The unpaired proton in the nitrogen can contribute to the asymmetry as well. The correction for this asymmetry is

$$-\frac{1}{3}\frac{1}{3}\frac{P_N}{P_p}g_{EMC}(x), \tag{15}$$

where the first factor of 1/3 is from Clebsch-Gordan coefficients, the second factor of 1/3 is because there are 3 hydrogen atoms for each nitrogen atom, P_N is the polarization of the nitrogen and P_p is the polarization of the hydrogen. The correction is approximately $(2 \pm 0.4)\%$ with only a weak x dependence.

Radiative corrections are also x dependent. We estimate this uncertainty based on the experience of E143 in which they varied their input models to their radiative correction algorithm and observe a 2.1% variation. However, the improvement in measurements of g_2 data in DIS and g_1 data in the resonance region make it reasonable to expect a 1.5% uncertainty in the radiative corrections.

There are nuclei inside the target other than hydrogen. The asymmetry from scattering off hydrogen is diluted by the scattering off these other nuclei. To calculate this dilution factor, we calculate the rates for the Born process:

$$\text{rate} \propto \rho z \left[ZF_2^p(x,Q^2) + NF_2^n(x,Q^2)\right] g_{EMC}(x,Q^2), \tag{16}$$

Table 7: Estimate systematic uncertainties in extracting A_1^p for $E = 6$ GeV. The uncertainties for $E = 4.8$ GeV are very similar.

	A_1^p		g_2^p	
	$x = 0.3$	$x = 0.6$	$x = 0.3$	$x = 0.6$
Radiative Corrections	1.5%	1.5%	1.5%	1.5%
Dilution Factor	2.0%	2.0%	2.0%	2.0%
Target Polarization	2.5%	2.5%	2.5%	2.5%
Beam Polarization	1.0%	1.0%	1.0%	1.0%
Nitrogen Correction	0.4%	0.4%	0.4%	0.4%
Kinematic Uncertainties	0.4%	0.5%	2.7%	4.5%
R	0.8%	1.2%	1.5%	1.3%
Background	1.0%	1.0%	3.7%	1.8%
Total	4.2%	4.0%	6.8%	6.7%

where ρ is the density of the material and z is the thickness. The dilution factor is then

$$f = \left(\frac{r_{pol}(x, Q^2)}{r_{pol} + \sum_i r_i} \right) \times r_c, \tag{17}$$

where r_{pol} is the rate for the polarized material and r_i is the rate for each of the unpolarized materials. The ratio of the neutron to proton structure functions is known to 1%. The uncertainty of the EMC effect is 1.5%, so that the overall uncertainty in the dilution factor is 2%.

The ratio of the unpolarized structure functions $R(x, Q^2)$ is involved in the extraction of A_1^p from the measured asymmetries. Typical uncertainties in R in this kinematic regime are 20% [43] which leads to a 1.5% uncertainty in A_1^p and g_2^p.

7 Projected Uncertainties

In this section, we will discuss the wealth of physics that can be harvested from SANE. We begin with a brief description of how we estimated the statistics for the measured asymmetries.

To estimate the statistical uncertainty, we used the MRST parameterization of the DIS structure functions. We incorporated into our simulation this cross section, a simple polynomial fit to existing A_1^p data and assumed that g_2=g_2^{WW}. We have assumed a beam current of 85 nA, an average target polarization of 75% and a beam polarization of 75%. All of the statistical uncertainties presented in this proposal have been calculated through the simulations package developed for this experiment. As a consequence, any inherent inefficiencies in the detector system are automatically taken into account.

As an example of the the projected uncertainties, we present in Table 8 the statistical uncertainties for DIS of the extracted A_1^p, A_2^p, g_1^p and g_2^p. The table list the uncertainties for both 4.8 and 6.0 GeV beam. The 6.0 GeV data has a larger x coverage in the DIS region.

Table 8: List of projected absolute statistical uncertainties in A_1, A_2, g_1 and g_2 for DIS ($W > 2$ GeV) for one possible choice of x binning. A cut of $33 \leq \theta_{scat} \leq 47$ was placed to ensure overlapping acceptance for the parallel and off-perpendicular measurements.

	$E = 4.8$ GeV				$E = 6.0$ GeV			
x	δA_1^p	δA_2^p	δg_1^p	δg_2^p	δA_1^p	δA_2^p	δg_1^p	δg_2^p
0.325	0.022	0.022	0.0085	0.0216	0.015	0.016	0.0059	0.0186
0.375	0.014	0.014	0.0043	0.0104	0.012	0.012	0.0036	0.0102
0.425	0.012	0.012	0.0030	0.0066	0.012	0.011	0.0027	0.0067
0.475	0.015	0.014	0.0028	0.0056	0.012	0.012	0.0021	0.0049
0.525	0.048	0.045	0.0071	0.0141	0.014	0.013	0.0017	0.0037
0.575					0.017	0.016	0.0015	0.0031
0.625					0.045	0.041	0.0028	0.0057

g_2 from SANE compared to World data

A comparison of the projected results for g_2 compared to the world's data is given in Fig. 15. This figure is a plot of $x^2 g_2$ versus x. The black points are the world's data, which is almost exclusively in the DIS region[6]. The red (green) points are the projected uncertainties from SANE for beam energy of 6.0 (4.8) GeV. The solid symbols denote SANE uncertainties in the DIS region, and the hollow ones are in the resonance region. Not only are the SANE data uncertainties smaller than the existing data, but the x binning of points is much smaller. In addition, the kinematics coverage of SANE is precisely where $x^2 g_2$ is the largest, and therefore the most important in determining third moments.

One of the important aspects of SANE is the nature in which the data is collected. Data for all momentum is collected simultaneously for a given target field direction. In this manner, the point-to-point systematics of SANE are significantly reduced. Thus, we can think of the SANE results as one body of data with a global normalization.

Q^2 dependence at fixed x

One of the great benefits of SANE is the large kinematic range covered with good statistics for the two beam energies, as seen in Fig. 16. This plots shows the projected statistics uncertainties binned in Q^2 and x for $x^2 g_1^p$ and $x^2 g_2^p$ for both beam energies. The range of kinematics covered by the two beam energies of SANE is situated where the curves are largest and most sensitive to Q^2. The two beam energies nicely complement each other. For example, for $Q^2 = 4$, the lower x half of the curved is covered by the 6.0 GeV data and the upper x half is covered by the 4.8 GeV data. It is quite clear from these plots that SANE will enable us to perform a Q^2 dependence study at fixed x, which will be a first for g_2.

In addition, the continuous coverage of the kinematic region of interest allows us to study the Q^2 dependence at fixed invariant mass W, as it can be seen in Fig. 3. This will let us follow the Q^2 behavior of specific regions of final state masses, to separate resonances and

[6]The RSS experiment will extract g_2 in the resonance region at a lower Q^2 than is accessible by SANE

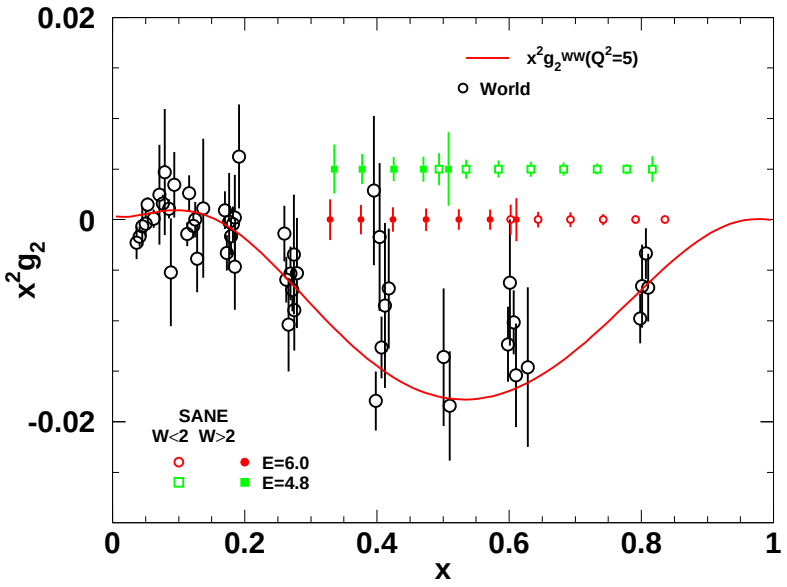

Figure 15: Comparison of World's data for x^2g_2 and the projected uncertainties from SANE. Also shown is the $x^2g_2^{WW}$ evaluated at $Q^2 = 5(\mathrm{GeV/c})^2$. See text for further description.

DIS contributions.

Third moments and d_2

SANE will provide unprecedented information on d_2. One can write d_2 as

$$d_2 = 3\int_0^1 dx\ x^2(g_2 - g_2^{WW}) = \int_0^1 dx\ x^2(3g_2 + 2g_1), \tag{18}$$

so that by measuring the third moments of g_1 and g_2 we can determine d_2. The quality of the data from SANE, as seen in Fig. 16, enables us to bin the SANE data in Q^2 bins of $\Delta Q^2 = 1$ (GeV/c)^2. Thus, we are able to extract the third moments and d_2 as a function of Q^2. In the fitting of the moments, we included the world's data when it fell within the Q^2 bin. This was particularly important in the low x region where SANE cannot provide data.[7] The total projected uncertainty from SANE in d_2 and the third moments of g_1 and g_2 is given in Table 9. We assumed that the systematic uncertainty is about one-half point-to-point and one-half normalization uncertainty. The normalization contribution essentially vanishes in the uncertainty in d_2. The systematic and statistical uncertainties are roughly equal for each of the Q^2 bins. These values are the uncertainties in d_2 evaluated at the Q^2, as opposed to the E155x results in which data from Q^2 of 1 to 8 (GeV/c)^2 are used to determine d_2.

A_1^p from SANE compared to World's data

In addition to the g_2 related results, SANE will be able to determine A_1^p. A plot of the

[7]It is also interesting to note that as seen in Fig. 16, there is very little Q^2 dependence for $x < 0.3$.

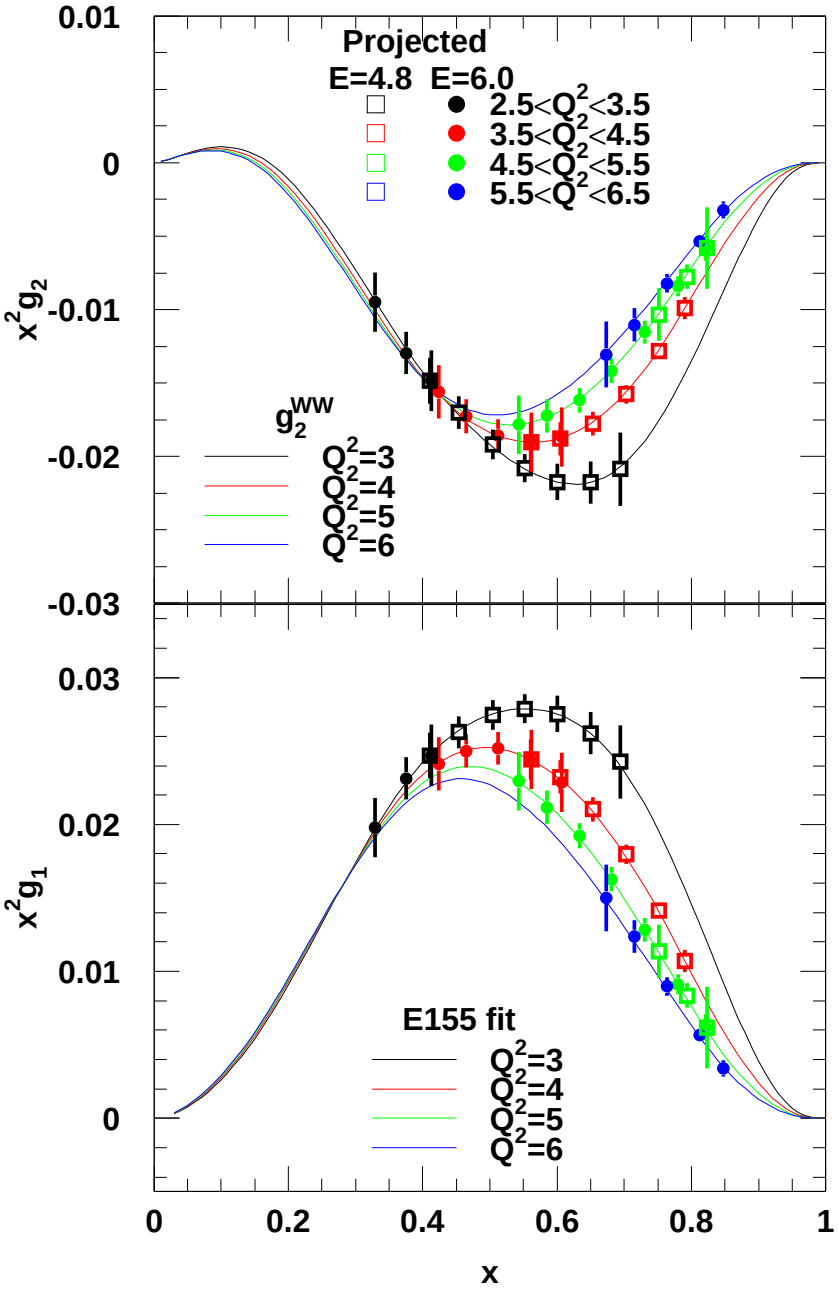

Figure 16: Statistical uncertainties in $x^2 g_2^p$ and $x^2 g_1^p$ in $\Delta Q^2 = 1(\mathrm{GeV/c})^2$ bins as a function of x. We used the E155 fit [44] to g_1/F_1 to calculate g_1 and g_2^{WW} for the solid lines. The projected uncertainties for 6.0 GeV are shown as solid circles and for 4.8 GeV as hollow squares.

Table 9: Table of projected uncertainties in d_2 and the third moments of g_1 and g_2. We show the values of the moments to demonstrate the possible Q^2 sensitivity. These values simply reflect the use of the A_1 fit from E155 and the assumption that $g_2 = g_2^{WW}$. The Lattice QCD calculation is from Ref. [45].

	Q^2	d_2	$\int dx x^2 g_2$	$\int dx x^2 g_1$
E155x	5	0.0032 ± 0.0017	-0.0072 ± 0.0006	-
Lattice	5	0.0085 ± 0.0035	-0.0100 ± 0.003	0.017 ± 0.004
SANE	3	$\pm$ 0.0010	$-0.0032 \pm$ 0.0003	$0.0055 \pm$ 0.0003
	4	$\pm$ 0.0007	$-0.0026 \pm$ 0.0002	$0.0049 \pm$ 0.0003
	5	$\pm$ 0.0007	$-0.0024 \pm$ 0.0003	$0.0043 \pm$ 0.0003
	6	$\pm$ 0.0010	$-0.0021 \pm$ 0.0003	$0.0042 \pm$ 0.0003

projected statistical error in A_1^p compared to the published world data is shown in Fig. 17. We show the projected results for both the DIS region and the resonance region, all of which is acquired simultaneously. Compared to existing world data, the projected uncertainties from SANE in A_1^p are exquisite.

The EG1b run group of CLAS does have a significant body of data from which they can extract A_1^p. One important aspect of SANE is the complementarity to this data. The EG1b data is taken with the target field parallel to the beam. The statistical uncertainties of this data are similar to SANE's up to $x \approx 0.5$, at which point the SANE uncertainties will be smaller. [42] The transverse target data from SANE would enable a model independent extraction of A_1 and g_1 from both the SANE and the CLAS data. This is particularly important in the resonance region, where there is a dearth of data with the notable exception of RSS.

A_1^p as $x \to 1$

The potential impact of the SANE data on our understanding of A_1^p as $x \to 1$ is demonstrated in Fig. 18. In this plot, we show the 1 σ error band of the fit to the existing world data for $x > 0.3$ to the functional form $A_1^p = x^a(b + cx^2)$. The second order polynomial allows for uncertainties in the extrapolation from the measured region of x to $x = 1$. It is clear that from the existing data we cannot distinguish the two possibilities of $A_1^p = 5/9$ and 1.

We must also consider the results coming from CLAS. The EG1b spokespersons have provided us with estimated statistical errors for a quantity that is A_1^p up to contributions from A_2^p. [42] For the sake of simplicity, we will ignore the uncertainties due to the A_2^p subtraction and assume that the EG1b point-to-point systematics are the same as SANE, i.e. approximately 3%. We randomize the CLAS data around the fit to the world's data by their estimated uncertainties and refit the World+CLAS data. Despite the lack of high x data from EG1b, the CLAS data reduces the uncertainty in the extrapolated A_1^p at $x \to 1$ to about 75% of the extrapolation to the World's data.

We repeat this process with the SANE projected DIS results. The world's published data

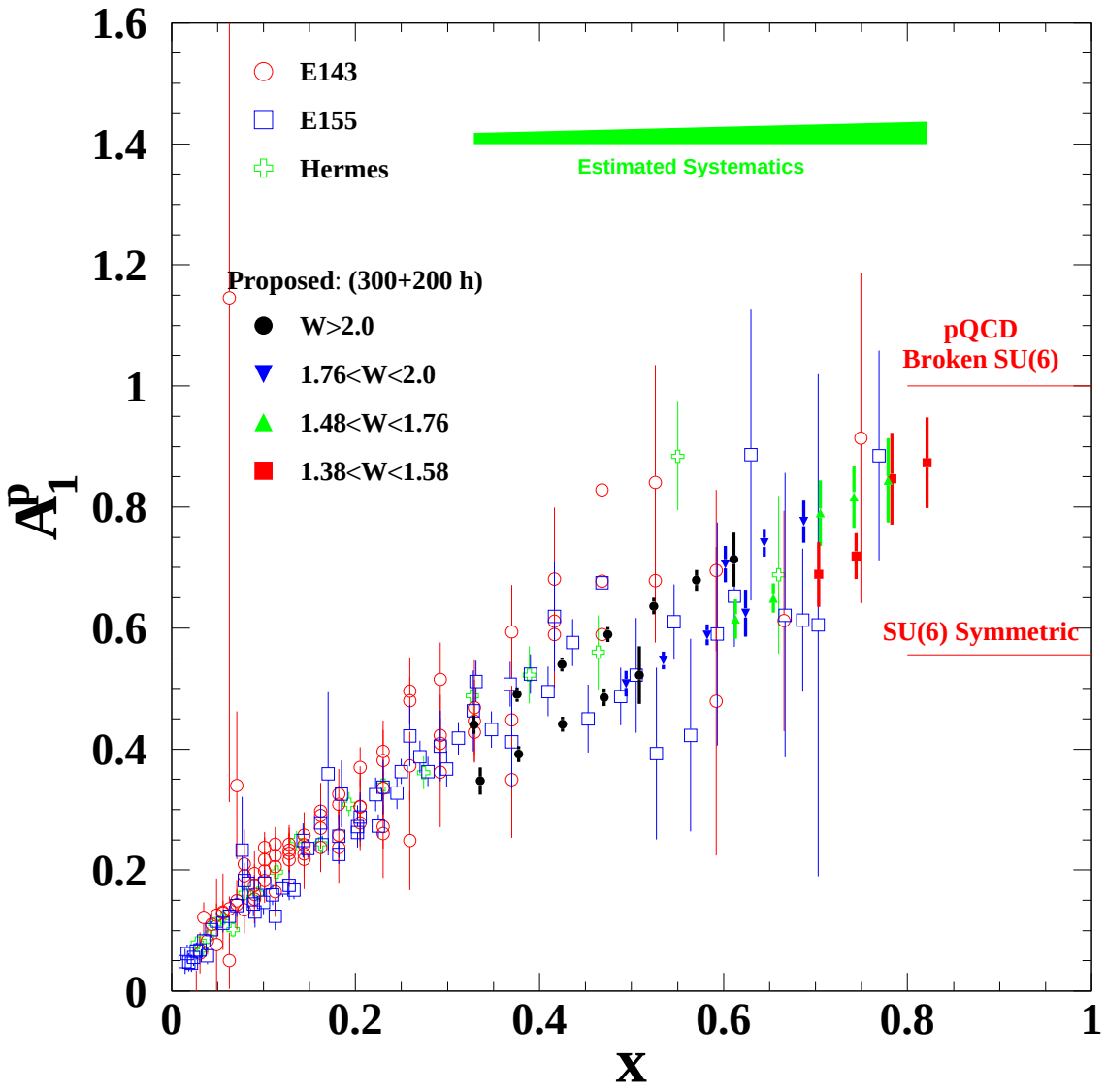

Figure 17: World's data for A_1^p for high x and our projected uncertainties for both beam energies. The top locus of points is for $E = 6$ GeV and the bottom locus is for $E = 4.8$ GeV. The $E = 4.8$ GeV points have been shifted down for clarity. The two horizontal lines extending below $x = 1$ represent the SU(6) symmetric and pQCD predictions for A_1^p at $x = 1$.

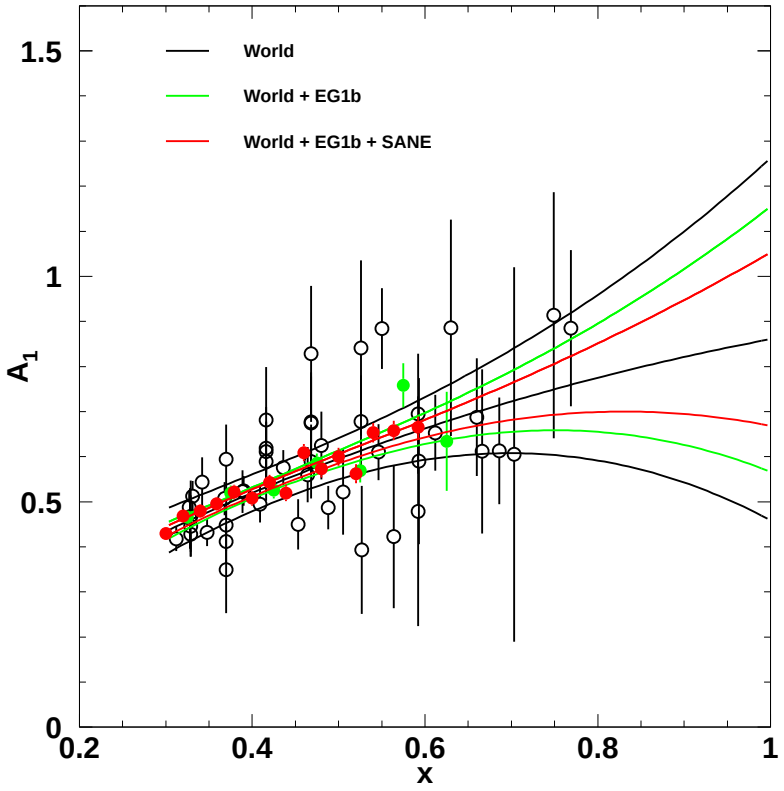

Figure 18: Demonstration of how different data sets may constrain our understanding of A_1^p as $x \to 1$. The black empty circles are the published world's data. The green circles are the estimated and randomized results from EG1b. The red circles are the projected and randomized results from SANE. See the text for a further description.

and the EG1b estimated data and the SANE projected data together reduce the uncertainty in A_1^p as $x \to 1$ by 50% compared to the fit to the world's data alone. It is worth mentioning that further improvement in the SANE statistical uncertainties beyond this proposal would not significantly reduce the uncertainty in A_1^p as $x \to 1$ because of the lack of significant statistics for $x > 0.6$ in the DIS region.

Limited Test of Local Duality

SANE will be able to conduct a limited test of local duality. The two beam energy measurements allows for a adequate range in W above about below 2 GeV to conduct this test. This capability is clearly demonstrated in Fig. 17. Should duality be demonstrated to be valid in this kinematic range for the spin structure functions, we will be able to extend the maximum x range of the data significantly. This extension would greatly enhance the lever arm of SANE in determining A_1^p as $x \to 1$.

Table 10: Summary of Time Requests.. The top portion lists the beam time requested, and the bottom portion lists time for configuration changes. The 2.4 GeV run is for calorimeter calibration. For the other measurements, the location of the HMS will vary to study the background rates and asymmetries.

E_{beam} (GeV)	I (nA)	θ_N (°)	θ_e (°)	Time (h)
6.0	85	180	40	100
6.0	85	80	40	200
4.8	85	180	40	70
4.8	85	80	40	130
2.4	1000	26	58	10
Packing Fraction				20
Moller Measurements				21
Beam Time				551
Target anneals				62
Energy change				48
Target Rotation				48
Stick Changes				48
Overhead Time				206
Requested Time				654

8 Beam Request

We propose to conduct asymmetry measurements at two beam energies, 4.8 and 6.0 GeV. A summary of the requested time is shown in Table 10. We require a 10 hours to calibrate the calorimeter with $e + p$ elastics. To measure the packing fraction of the material in the cup, we need 20 hours to do empty cell and carbon measurements. We also request one hour per day of polarized running to measure the beam polarization with the Moller polarimeter.

Also shown in Table 10 is a summary of the time required for configuration changes. We request 3 hours per day of asymmetry measurements (i.e. not including the calibration runs) to perform anneals of the target to restore the target polarization. We also include one day per beam energy change. We will need to change the target stick four times to load fresh material. Each of these changes will take about twelve hours to change the material and perform new target polarization calibrations. During the change from $E = 2.4$ GeV to higher beam energy, we will rotate the target magnet. We will need to rotate the target field twice which will take about one day per rotation.

The total time requested is a combination of the required beam time and the overhead time. From experience running G_{En} and RSS, we know that roughly one-half of the overhead can be performed during times when the accelerator is not delivering physics beam to the Halls. Thus, our total requested time is the sum of the beam time and one-half of the overhead time.

This experiment requires extensive support from the JLab. In addition to the installation of the polarized target, we will also require:

- installation of the Secondary Emission Monitor (SEM),
- beam line instrumentation workable down to 50 nA beam current,
- the two upstream chicane magnets so that the beam is horizontal in the middle of the target,
- the large slow raster that distributes the beam uniformly on the surface of the target,
- a special dump in the hall for when the beam is deflected during the non-parallel target field measurements.

These are the same requirements as for the G_{En} and RSS experiment that ran from Aug. 2001 through March 2002, so they present no special development for the laboratory.

We would to note that the HMS will be used by SANE only about one-half of the time to study background. The balance of the time it would be available to perform other physics, either single-arm or coincidence.

9 Collaboration

The SANE collaboration consists of members with extensive experience using the UVa polarized target in Hall C, in conducting high x measurements on the neutron in Hall A as well as spin structure function measurements at SLAC and in electromagnetic calorimetry. Various members of the collaboration have expressed an interest in playing a leading role in the design and development of the various elements of BETA. We anticipate that under a similar arrangement as for G_{En} and RSS, the JLab target group together with the UVa polarized target group will handle installation, calibration and operation of the polarized target.

10 Acknowledgments

The authors wish to thank John Arrington and Wally Melnitchouk for the useful and insightful comments in preparing this document. We also wish to thank Sebastian Kuhn, Volker Burkert and Peter Bosted for their discussion of the EG1 data and for providing the estimated statistical uncertainties.

References

[1] J. Negele, private communication.

[2] C. E. Carlson and Wu-Ki Tung, Phys. Rev. D **5** (1972) 721.

[3] A. J. G. Hey and J. E. Mandula, Phys. Rev. D **5** (1972) 2610.

[4] S. Wandzura and F. Wilczek, Phys. Lett. B172 (1977) 195.

[5] J. L. Cortes, B. Pire and J. P. Ralston, Z. Phys. C55 (1992) 409.

[6] R. L. Jaffe and Xiangdong Ji, Phys. Rev. **D 67** (1991) 552.

[7] SLAC E80, M. J. Alguard *et al.*, Phys. Rev. Lett. **37**, 1261 (1976); **41**, 70 (1978).

[8] SLAC E130, G. Baum *et al.*, Phys. Rev. Lett. **51**, 1135 (1983).

[9] EMC, J. Ashman *et al.*, Nucl. Phys. **B328**, 1 (1989)

[10] SLAC E142, P. L. Anthony *et al.*, Phys. Rev. Lett. **71**, 959 (1993).

[11] SLAC E143, K. Abe *et al.*, Phys. Rev. D **58**, 112003 (1998).

[12] SMC, B. Adeva *et al.*, Phys. Rev. D **58** 112001-1 (1998).

[13] SLAC E154, K. Abe *et al.*, Phys. Rev Lett. 79 (1997) 26.

[14] SLAC E155, K. Abe *et al.*, Phys. Lett. **B463**, 339 (1999).

[15] P. L. Anthony *et al.*[E155 Collaboration], Phys. Lett. **B553**, 18 (2003).

[16] A. Airapetian *et al.*[HERMES Collaboration], Phys. Lett. **B442**, 484 (1998).

[17] G. Cates, J.P. Chen, Z-E. Meziani, spokespersons *Measurement of the Neutron (^{3}He) Spin Structure Function at Low Q^2: a Connection between the Bjorken and Drell- Hearn-Gerasimov Sum Rules*, CEBAF experiment 94-010.

[18] V. Burkert, D. Crabb, R. Minehart, spokespersons, *Measurement of Polarized Structure Functions in Inelastic Electron Proton Scattering using CLAS*, CEBAF Experiment 91-023.

[19] S.E. Kuhn, spokesperson, *The Polarized Structure Function g_l^n and the Q^2 dependence of the Gerasimov-Drell-Hearn Sum Rule for the Neutron*, CEBAF Experiment 93-009.

[20] Todd Averett, Wolfgang Korsch, spokespersons, *Search for Higher Twist Effects in the Neutron Spin Structure Function g2n(x,Q2)*,JLab Experiment 97-103.

[21] J. P. Chen, Z-E. Meziani, P. Souder, spokespersons, *Precision Measurement of the Neutron Asymmetry A1n at Large x using CEBAF at 6 GeV*, JLab Experiment 99-117.

[22] O. A. Rondon, spokesperson, *Precision Measurement of the Nucleon Spin Structure Functions in the Region of the Nucleon Resonances*, JLab Experiment 01-006.

[23] R. Van de Vyver [A2/GDH Collaboration], Nucl. Phys. A **689**, 379 (2001).

[24] K. Helbing [GDH Collaboration], "Status of the GDH experiment at ELSA", Published in Mainz 2000, Gerasimov-Drell-Hearn sum rule and the nucleon spin structure in the resonance region, p. 133

[25] S. Brodsky, M. Burkardt, and I. Schmidt, Nucl. Phys. **B441**, 197 (1995).

[26] N. Isgur, Phys. Rev. D **59**, 034013 (1999)

[27] G. R. Farrar and D. R. Jackson, Phys. Rev. Lett. **35**, 1416 (1975);
J. F. Gunion, P. Nason and R. Blankenbecler, Phys. Rev. D **29**, 2491 (1984).

[28] J. McCarthy, O. A. Rondon and T. J. Liu, Phys. Rev. D **54**, 2391 (1996).

[29] W. Alexander Tobias, *Measurement of the Proton and Deuteron Spin Structure Functions g_1 and g_2*, Ph. D. Thesis, Charlottesville, 1999, unpublished

[30] E. Shuryak and A. Vainshtein, Nucl. Phys. B**201** (1982) 141.

[31] E. Stein, P. Gornicki, L. Mankiewicz and A. Schafer, Phys. Lett. B **353**, 107 (1995);
E. V. Shuryak and A. I. Vainshtein, Nucl. Phys. B **201**, 141 (1982);
Philippe Grenier, *Etude des Fonctions de Structure en Spin du Nucleon: L'Experience E143 au SLAC*, Ph. D. Thesis, Saclay 1995, unpublished.

[32] M. Anselmino, A. Efremov and E. Leader, Phys. Rep. **261**, 1 (1995).

[33] B. Kross, private communication.

[34] M. Buenerd, "Study of the Background in the E154 Data", April 22, 1996. Unpublished.

[35] W. Hinton, "Quasi-free electroproduction of Λ, Σ^0, and Σ^- Hyperons on Carbon and Aluminum", Hampton University, December 2000, unpublished.

[36] A. Dzierba, J. Napolitano, spokespersons, *A Measurement of Rare Radiative Decays of the ϕ Meson*, JLab Experiment E94-016.

[37] R. Crittenden *et al.*, NIM A 387 (1997) 377-394; also Scott Teige, Indiana University, private communication.

[38] A.D. Martin *et al.*, hep-ph/0110215.

[39] J. Arrington, private communication (2002).

[40] J.W. Lightbody and J.S. O'Connell, Computers in Physics, 58 (1988).

[41] X. Zheng, memo to E99-117 collaboration, Sept. 5, 2000.

[42] P. Bosted, private communication (2002).

[43] L.H. Tao *et al.*, Z. Phys. C **70**, 387 (1996).

[44] P.L. Anthony *et al.*, Phys. Lett. B **493**, 19 (2000).

[45] M. Göckeler *et al.*, Phys. Rev. D **63** 074506 (2001).